# Abstract

Cemented carbides (WC-Co) are ceramic-metal composite materials made by hard tungsten carbide particles bonded through a metallic binder matrix, mainly of cobalt. It is a hard material characterized by an exceptional combination of strength, toughness and wear resistance. As result, cemented carbides are first choice materials for cutting tools and wear parts. However, final shaping of these components usually require diamond grinding. During this hard machining, surface integrity may became altered, particulary in terms of compression stresses and/or microcracking. Such defects can locally affect the mechanical properties.

The aim of this investigation is to analyze the influence of the surface finish quality on the mechanical properties at the surface level for WC-Co materials as well as the influence over the properties of a TiN coating deposited on hardmetal substrates.

The study has been done at micrometric (to analyze the general properties) and nanometric scale (local properties aiming to capture residual stress state effects) by using nanoindentation and nanoscratch testing. Tests done in plain view prove that roughness plays an important role in the assessment of mechanical properties at the surface, as it induces significant scatter, as compared to results determined on cross-sections.

Finally, a sequential polishing process has been done in order to extract the polishing rate for cemented materials as well as study how roughness affects the mechanical properties measured. This process points out that roughness can mask surface damage, like cracks or chipping, among others.

As a final conclusion, an optimized protocol is proposed to study the mechanical properties of the samples with high roughness and exhibiting a compressive residual stress state.

# Glossary

| | |
|---|---|
| **A:** | Contact radius |
| **$A_c$:** | Projected contact area |
| **AFM** | Atomic Force Microscopy |
| **AR:** | As received |
| **$\sigma_c$:** | Compressions stresses |
| **CSM:** | Continuous stiffness measurement |
| **D:** | Tip indenter diameter |
| **$\epsilon$:** | Constant function on the geometry indenter |
| **E:** | Young's Modulus or indentation elastic modulus |
| **$E_{eff}$:** | Effective Young's modulus or indentation effective elastic modulus |
| **$E_i$:** | Indenter Young's modulus |
| **$E_m$:** | Material Young's modulus |
| **FESEM** | Field Emission Scanning Electron Microscopy |
| **G:** | Ground |
| **G+TT:** | Ground with thermal treatment |
| **H:** | Hardness |
| **$h_c$:** | Contact penetration depth |
| **$h_e$:** | Elastic penetration depth |
| **HIP** | Hot Isostatic Pressing |
| **$h_{max}$:** | Maximum displacement into surface |
| **HV:** | Vickers' Hardness |
| **IE:** | Ion-etched |
| **IIT:** | Instrumented Indentation Technique |

| | |
|---|---|
| **LSCM** | Laser Scanning Confocal Microscope |
| **$P_{150}$:** | Samples with the polishing process done by SecoTools |
| **$P_{max}$:** | Maximum applied load |
| **$P_{UPC}$:** | Mirror-like polished samples |
| **R:** | Radius indenter |
| **S:** | Slope on the linear part in the unloanding curve or Stiffness |
| **$v_i$:** | Indenter Poisson's ratio |
| **$v_m$:** | Material Poisson's ratio |
| **XRD:** | X-Ray Diffraction |

# Table of contents

Abstract ..... 1
Table of contents ..... 5
1. Introduction ..... 7
1.1. WC-Co Cemented Carbides: Hardmetals ..... 7
1.1.1. Properties ..... 8
1.1.1 Manufacturing process ..... 11
1.1.2 WC-Co hardmetal grades ..... 12
1.1.3 Applications ..... 13
1.1.4. Recycling ..... 14
1.2. Mechanical characterization ..... 15
1.2.1. Vickers Hardness Testing ..... 16
1.2.2. Mechanical characterization: Nanoindentation Test ..... 16
1.2.2.1. Advantages and Disadvantages of IIT. ..... 17
1.2.2.2. Tip of the indenter ..... 18
1.2.2.3. Contact Mechanics ..... 19
(a) Elastic contact: Hertz equations ..... 19
(b) Elasto-plastic contact: Oliver and Pharr equations ..... 21
1.3. Sliding contact response: Nanoscratch test ..... 23
1.4. Range of mechanical properties for hardmetal substrate and TiN coating. ..... 25
2. Objectives ..... 27
3. Experimental procedure ..... 28
3.1. Material and surface finish conditions ..... 28
3.2. Sample preparation ..... 29
3.2.1. Plain view testing ..... 29
3.2.2. Cross-section testing ..... 29
3.3. Mechanical characterization ..... 30
3.2.1. Microhardness tests: Vickers Hardness ..... 30
3.2.2. Polishing rate ..... 30
3.4. Instrumented indentation ..... 32

3.5. Nanoscratch testing ..... 34
3.6. Surface characterization ..... 35
3.6.1. Laser scanning confocal microscope, LSCM ..... 35
3.6.2. Field emission scanning electron microscopy, FESEM ..... 36
3.6.3. Atomic force microscopy, AFM ..... 37
4. Results and discussion ..... 38
4.1. Residual stresses at the surface, as induced by grinding ..... 38
4.2. Mechanical properties: ..... 39
4.2.1. Plain view ..... 39
4.2.1.1. Microindentation ..... 39
4.2.1.2. Nanoindentation ..... 48
4.2.1.3. Nanoscratch ..... 54
4.2.2. Cross-section testing ..... 58
5. Protocol proposed to mechanical characterization of surface integrity. ..... 69
6. Conclusions ..... 70
7. Proposals for futures studies ..... 71
8. Environmental impact ..... 72
9. Economical cost ..... 73
10. Acknowledgements ..... 74
11. References ..... 75

# 1. Introduction

## 1.1. WC-Co Cemented Carbides: Hardmetals

WC-Co Cemented carbides or hardmetals are ceramic-metal composite materials made by hard tungsten carbide particles bonded through a metallic binder matrix, see **Figure 1.1**. As a result, an heterogeneous composite is obtained with a weight fraction of the ceramic phase between 70-97% and a grain size distribution ranging from 0.4 to 10 µm [1].

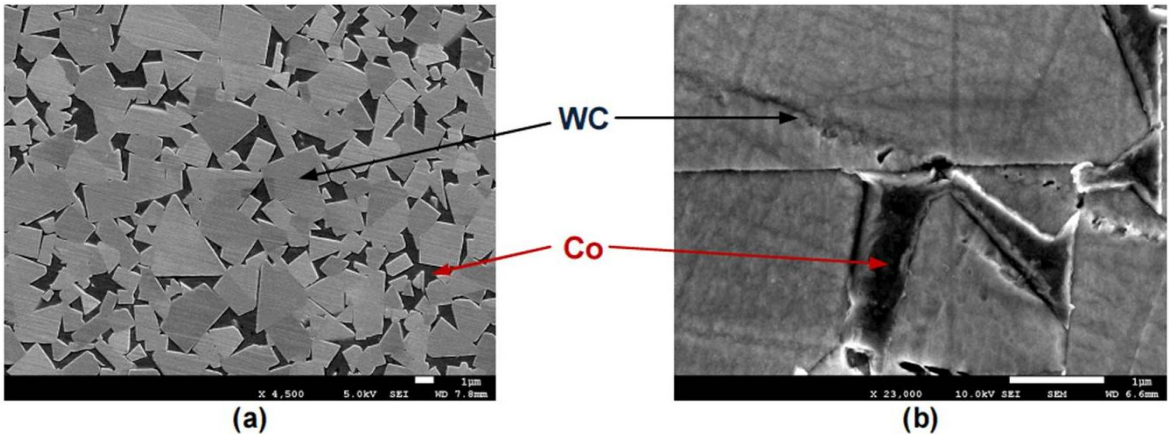


**Figure 1.1:** SEM micrograph of a typical microstructure of a hardmetal [2].
**(a)** Particles of tungsten carbides within a binder phase, and **(b)** Magnification showing the interface between the ceramic particles and the metallic binder.

The combination of these two phases leads to a material with outstanding mechanical properties that combine the typical properties of ceramics, such as high hardness, wear resistance and chemical stability, with the toughness and good thermal conductivity of metallic materials [3].

The elevated hardness of the WC-Co is comparable to that exhibited by diamond (see **Figure 1.2**). It is the main reason for being usually referred to as WIDIA (the acronyms for “wie Diamant”, in German: “like diamond”).

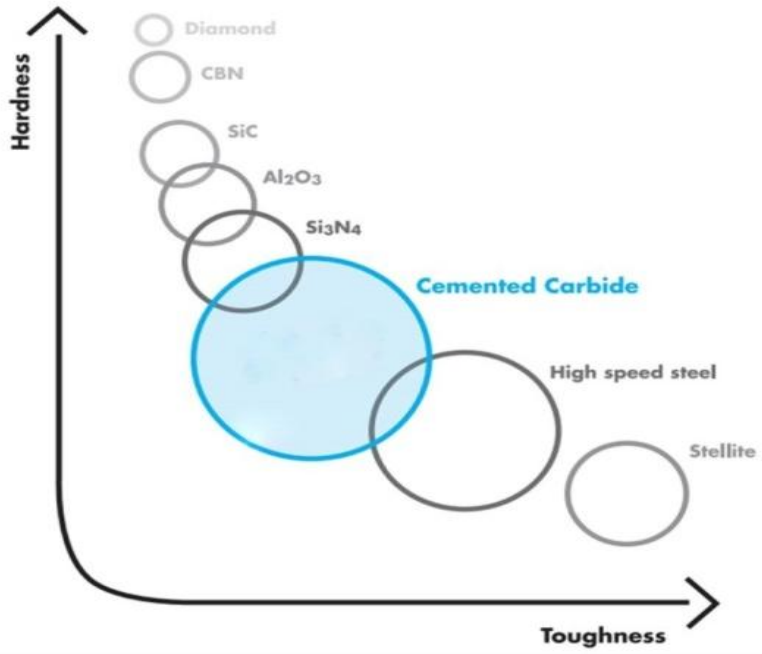


**Figure 1.2:** Illustration of the position of cemented carbide amongst others hard materials [1].

Due to the referred properties, WC-Co is the most used material for metalworking. Within this framework, cutting tools for solid end milling, hole-making, milling, tapping and tooling systems are the main applications of hardmetals [4].

### 1.1.1. Properties

Some of the most important properties of WC-Co are hardness, strength, toughness and wear resistance. These properties, especially hardness and toughness, are highly dependent on the nature, content and size of each microstructural constituent. Thus, by varying the metallic cobalt content and the tungsten carbide grain size, properties can be strongly modified, as it can be appreciated in **Table 1.1**.

**Table 1.1:** Properties for different types of WC-Co [5].

| Grade (wt %) | HV 30 | $\sigma_c$ (MPa) | TRS (MPa) | E (GPa) | $K_{Ic}$ (MPa·m$^{1/2}$) | $\alpha \cdot 10^{-6}$ ($K^{-1}$) |
|---|---|---|---|---|---|---|
| **WC-4Co** | 2000 | 7100 | 2000 | 665 | 8.5 | 5.0 |
| **WC-6Co/S*** | 1800 | 6000 | 3000 | 630 | 10.8 | 6.2 |
| **WC-6Co/M**** | 1580 | 5400 | 2000 | 630 | 9.6 | 5.5 |
| **WC-6Co/C***** | 1400 | 5000 | 2500 | 620 | 12.8 | 5.5 |
| **WC-25Co/M** | 780 | 3100 | 2900 | 470 | 14.5 | 7.5 |
| **WC-6Co-9,5(Ti,Ta,Nb)C** | 1700 | 5950 | 1750 | 580 | 9.0 | 6.0 |
| **WC-9Co-31(Ti,Ta,Nb)C** | 1560 | 4500 | 1700 | 520 | 8.1 | 7.2 |

**S*: submicron, M**: fine/medium; C***: coarse**

Vickers Hardness (HV 30); Compressive strength ($\sigma_c$); Transverse rupture strength (TRS); Young's modulus (E); Fracture toughness ($K_{IC}$); Thermal expansion coefficient (α)

As it can be seen in **Table 1.1** and in **Figure 1.3 (a)**, the finer the carbide grain, the higher is its hardness. By varying the cobalt content between 0 and 25 weight per cent (wt. %), hardmetals can cover a hardness range from super-hard materials to tempered steels. Moreover, they exhibit a Young's modulus 2-3 times higher than that of steels, and it decreases with %Co content (contrary to its Poisson's ratio) [6].

As can be appreciated in **Figure 1.3**, the volume or weight fraction (wt. %) of each phase is one of the most important factors for determining the influence of microstructure on the mechanical properties of cemented carbides.

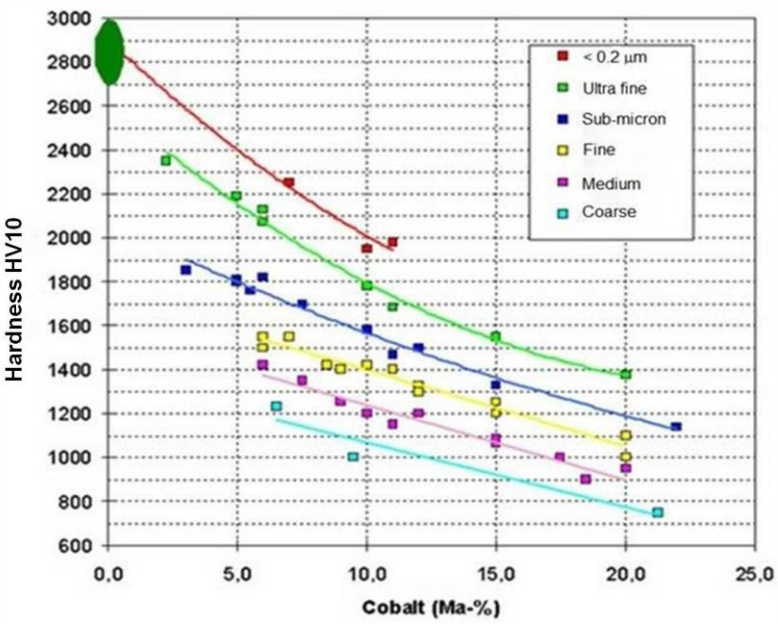


a)

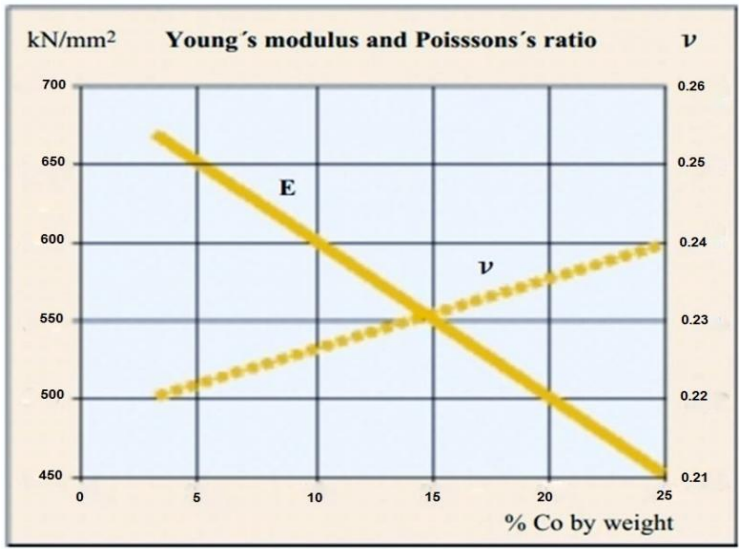


b)

**Figure 1.3:** Mechanical properties as a function of the cobalt content (wt. %) for hardmetals. **(a)** Vickers Hardness [2] and **(b)** Young's modulus and Poisson's ratio [1].

### 1.1.1 Manufacturing process

Hardmetals such as WC-Co composites are man-made materials. They are produced by mixing ceramic carbides and metal powders, followed by pressing and sintering. It involves several steps, as follows:

i) powder preparation,
ii) powder compaction,
iii) densification process by liquid-phase sintering, and
iv) post-treatment

There are many possible methods to produce tungsten carbide. It can be prepared by reaction of tungsten metal and carbon at high temperature (1400–2000 °C) [7]. Moreover, it can be produced by heating $WO_3$ with graphite (directly at 900 °C) or in hydrogen atmosphere (at 670 °C following by carburization in Ar at 1000 °C) [8].

Afterwards, cobalt should be added to tungsten carbide powder in a homogeneous way. Cobalt is mixed together with some extra components such as lubricants that ensure the homogeneity of cobalt in WC and avoid porosity. Then, powder needs to be dried. After sieving, the powder is pressed at about 274 MPa, green-machined and sintered at high temperatures (1350-1500 °C). At this range of temperature, cobalt (which has a high wettability in WC) is liquid and is able to accelerate densification of samples until obtaining 100% of theoretical density (liquid cobalt allows to wet WC particles, reducing its porosity). Machining of the part is usually done for cutting and forming tools, and frequently such a process is finished by coating the pieces. Then, quality control is required to certify the final products. **Figure 1.4** shows the sequential steps involving the production process of cemented carbides.

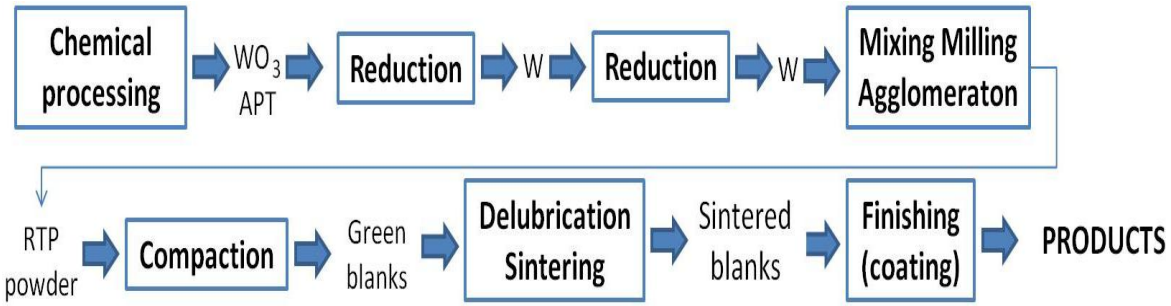


**Figure 1.4:** The processing steps in the production of WC-Co composites [9].

### 1.1.2 WC-Co hardmetal grades

There is a huge range of carbide grain sizes, which embraces from ultrafine grains to extracoarse ones (see **Figure 1.5**). The growth of WC crystals in each grade depends on the mean size and the size distribution of the starting powders, milling and sintering conditions, and composition of the binder. It is interesting to remark that high carbon contents generally promote the growth of tungsten carbide grains. Chromium carbide ($Cr_3C$) and vanadium carbide (VC) are generally required in the finest microstructure to avoid grain growth and to assure a uniform grain size distribution [10].

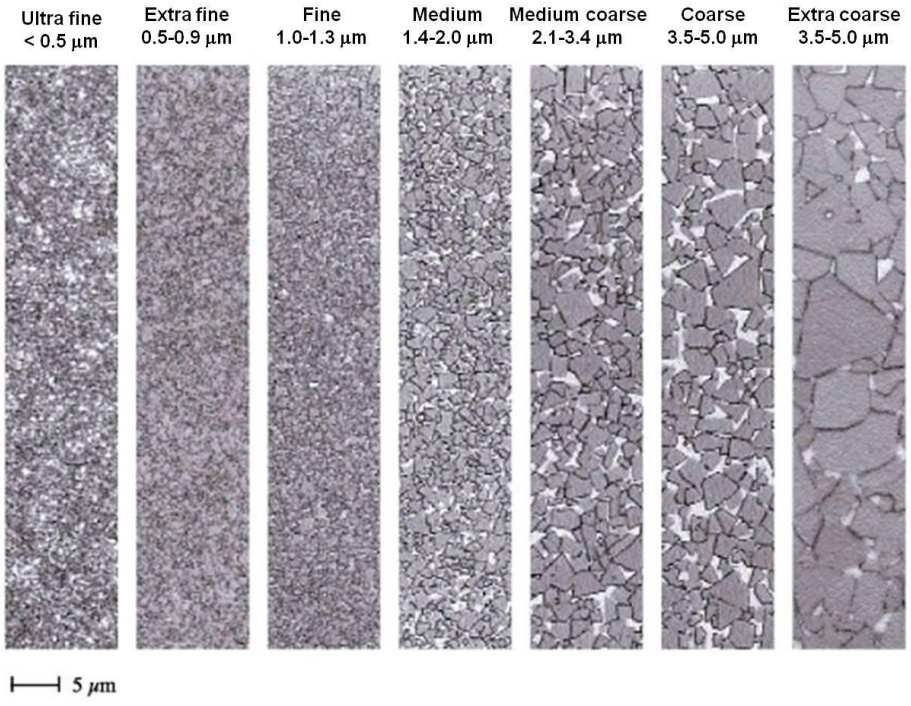


**Figure 1.5:** Grain size classification of cemented carbides [10].

### 1.1.3 Applications

Cemented carbides have a large range of industrial applications, depending on the WC-grain size as well as the Co content, see **Figure 1.6**.

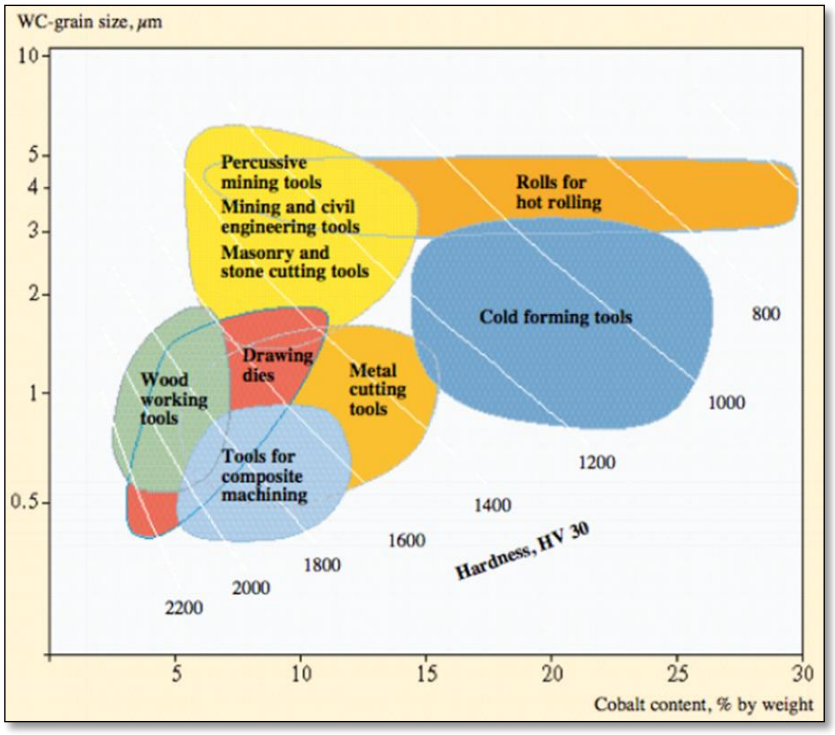


**Figure 1.6:** Application range in function of WC-grain size and Co content (%wt.) [1].

As it can be appreciated in **Figure 1.6**, the most important technical application is their use as cutting tools. However, hardmetals are also used for metal forming, composite machining, oil and gas drilling as well as mining tools [11]. Because of its wear resistance, WC-Co hardmetals are used in parts subjected to cyclic loading and temperature changes [12]. Likewise, different technical wear-resistant parts like nozzles or reinforcements are made of WC-Co composites as well as hardmetal drillers or hardmetal coated circular saw blades for hobby craftsmen, see **Figure 1.7**.

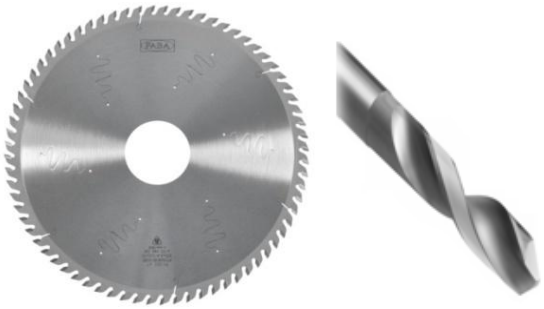

a ) b)

**Figure 1.7:** Example of different applications of WC-Co

**(a)** circular saw blades [13] and **(b)** drilling tool [1].

According to data gathered from literature, almost 26% of total production of cemented carbides is used for mining, oil drilling and tunneling industries, 22% for cutting tools and 26% and 9% for wood working and construction industries, respectively [9]. New applications are constantly being identified for these materials because their extraordinary combination of abrasion resistance, thermal shock resistance, mechanical impact strength, compressive strength, high elastic modulus and corrosion resistance [**¡Error! Marcador no definido.**].

### 1.1.4. Recycling

After usage and at the end of life cycle, cemented carbides are being recycled to a large extent. In case of scrap containing WC-Co hardmetals, it can be either fully processed (and re-enter the hardmetal production) or used for the production of various steel alloys, i.e.: high-speed steel.

The $2 billion worldwide tungsten carbide industry generates large quantities of scrap due to the rejected parts at various stages of production and the worn out tools and components. The most basic recycling approach would be to break down the scrap pieces into powders and then fabricate more WC-base cutting tools. This approach would cause severe equipment wear due to the abrasive nature of the cutting tool materials and therefore it is not feasible. As a result, the recycling is done by chemical means, such as the zinc recovery process, electrolytic recovery, and extraction by oxidation [14]. However, the zinc recovery process is a costly process and requires huge investment.

## 1.2. Mechanical characterization

Hardness, transverse rupture strength, compressive strength, elasticity modulus, fracture toughness and fatigue strength are some of the mechanical properties that are usually characterized WC-Co materials. On this project, we will focus in Hardness and Elastic modulus at micro- and nanomètric length scale.

Hardness (*H*) can be defined as the resistance of a material to be plastically deformed as it is indented. It can be determined by measuring the length of the imprint caused by the indentation of a tip. Results of this test critically depend on the surface preparation and on residual stress state at the surface.

Hardness can be measured with many different indentation methods that depend specially on the geometry of the indenter, see **Figure 1.8**:

- **Vickers hardness (HV):** It is based on indenting the surface with a diamond pyramid tip, see **Figure 1.8a**. The hardness is inversely proportional to the size of the impression and it is calculated by measuring the length of the diagonals of the imprint.

- **Rockwell hardness (HR):** This method is similar to Vickers hardness, but is based on the use of a diamond cone and the depth of the indentation is used as a measure of the hardness, see **Figure 1.8b.** Different indenters are used in function of the material to be indented. Moreover, there exist several scales. However the most common ones used for hardmetals are:: Rockwell C (HRC) and Rockwell B (HRB) [15].

- **Knoop hardness (HK):** It is used for very brittle materials or thin sheets, where only a small indentation may be made for testing purposes. The geometry of this indenter is an extended pyramid with length to width ratio of 7:1 and respective face angles of 172º for the long edge and 130º for the short one, see **Figure 1.8c**.

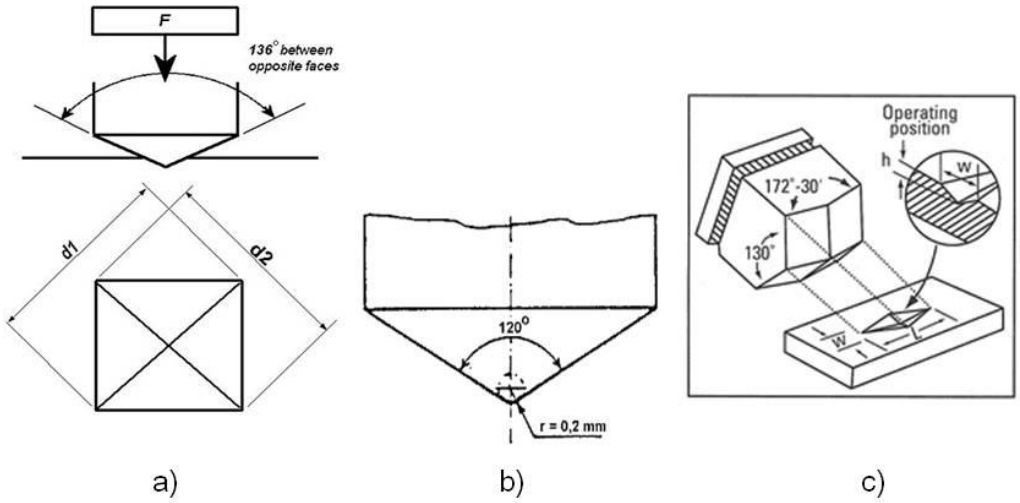


**Figure 1.8:** Scheme of the (a) Vickers, (b) Rockwell and (c) Knoop indenters [16].

## 1.2.1. Vickers Hardness Testing

During the Vickers hardness testing, a square base pyramid shaped diamond is used for the test and a large range of loads can be used (from 1gf to 150Kgf). For the calculation of the Vickers hardness, the following expression is used:

$$HV = \frac{1.854P}{d^2} \qquad \textbf{(ec. 1.1)}$$

where *P* is the applied load (in Kgf) and *d* the average length (mm) of the diagonals of the imprint left by the indenter after unloading.

## 1.2.2. Mechanical characterization: Nanoindentation Test

Nanoindentation test or Instrumented Indentation Technique (IIT) is used for the measurement of mechanical properties (such as Hardness and Elastic modulus) at micro- and nanometric-length-scale. These properties can be extracted directly from the load vs. displacement curves (*P-h* or loading-unloading) recorded during the test. The most common indenter used at this scale is a triangular pyramid-shaped known as Berkovich tip indenter. The position of the indenter is determined by a capacitance displacement gauge, and the force imposed can be changed by varying the current in the coil [17]. For

the equipment used in this study, 650 mN is the maximum peak load and 2000 nm is the maximum indentation depth. A scheme of the nanoindenter is given in **Figure 1.9**.

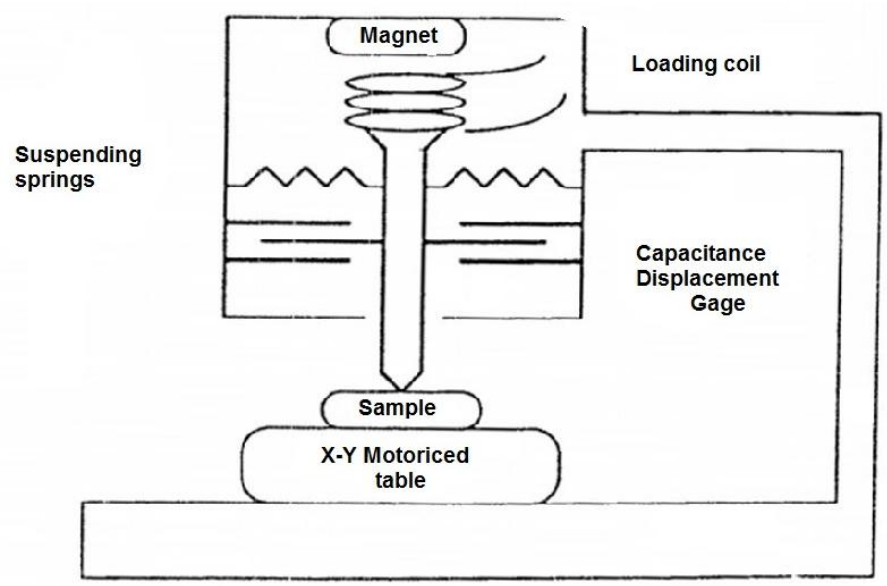


**Figure 1.9:** Schematic diagram of the indenting mechanism of the Nanoindenter [17].

The size of the residual impression done by using this technique is often only a few nanometers deep. It makes very difficult to obtain a direct measure of the contact area using optical techniques. Hence, the depth of penetration beneath the specimen surface is directly measured as the load is applied to the indenter, see **Figure 1.11**.

### 1.2.2.1. Advantages and Disadvantages of IIT.

Main advantages and disadvantages of ITT technique with respect to conventional techniques to extract the mechanical properties (mainly hardness), at macro- and micrometric length scale, are described in this section.

**Advantages**

- possible assessment of the mechanical response of different phases (e.g. inclusions, among others) at small length scale;

- effective simultaneous determination of hardness and elastic modulus; and

- possible measurement of the residual imprint produced during the test, without explicit need of visualizing it.

**Disadvantages**

- requirement of a calibration using a standard specimen (fused silica), in order to perfectly calibrate and know the shape of the indenter area;

- the quality of the surface to indent should be completely flat (several nm rough) in order to reduce the problems of the correct determination of the contact point;

- strict need of knowledge of the Poisson's ratio of the specimen, in order to determine the elastic modulus of the material of interest; and

- possible problems related with the nature of the material of interest, producing an under- or overestimation of the contact area: pile-up and sink-in effect in ductile and brittle materials, respectively.

### 1.2.2.2. Tip of the indenter

The indenter tip can be made of different materials, being diamond the most used one. However, it can also be made of tungsten carbide, hardened steel or even sapphire. Different indenters are used for characterizing different mechanical properties of materials. These indenters can be classified in ***four different groups*** depending on the characteristics of the tip:

- **Pyramidal indenters:** The Vickers indenter (used for microhardness tests) and the Berkovich indenter (for nanoindentation) belong to this group. The Berkovich indenter is a three-sided pyramid with the same depth-to-area relation as the Vickers indenter. It allows simultaneous measurement of hardness and elastic modulus [18].

- **Spherical and conical indenters:** For these indenters, the contact stress is initially small and products only elastic deformation. As the spherical indenter is driven into the surface, a transition from elastic to elasto-plastic deformation occurs. Elastic modulus, yield stress, mean contact pressure and strain-hardening behavior of a material can be determined using this kind of indenters [18].

- **Cube-corner indenters:** It is a three sided pyramid with mutually perpendicular faces arranged in a geometry like the corner of a cube. The centerline-to-face angle for this indenter is 34.3°. The sharpness of the cube corner produces much higher stresses and strains in the area of the contact. This is useful for producing very small, well-defined cracks around hardness impressions in brittle materials, which allows then to estimate fracture toughness at very small scales [19].

- **Flat punch:** The contact area is a flat-plane and it used for to investigate the viscoelastic response under quasi-static and dynamic loading conditions.

#### 1.2.2.3. Contact Mechanics

### (a) Elastic contact: Hertz equations

Hertz formulated elastic equations for spherical surface contact in the latter part of the 19$^{th}$ century. The model here described is essentially to study the elastic to elasto-plastic transition, and is based upon previous developments of others in the field, especially Hertbert *et al.* [20].

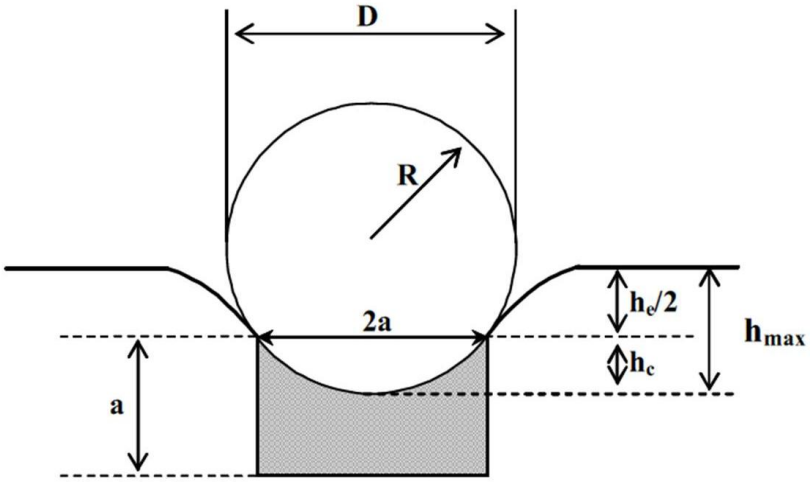


**Figure 1.10:** Spherical indentation scheme [21], where *D* is the tip indenter diameter, $h_e$ is the elastic contact depth, $h_c$ is the contact penetration depth, and *a* is the contact radius.

Analytical theory related to spherical nanoindentation is mostly based on the Hertz equation [22] in the elastic region. The pure elastic contact (or the initial nm in the loading curve) can be adjusted using the following equation:

$$P = \left(\frac{3}{4} E_{eff} R^{\frac{1}{2}}\right) {h_e}^{3/2} \qquad \textbf{(eq. 1.2)}$$

where *R* is the radius of the indenter, $h_e$ is the elastic penetration depth into the surface, and $E_{eff}$ is the effective Young's modulus, which can be directly determined using the following expression:

$$\frac{1}{E_{eff}} = \frac{(1-{\nu_m}^2)}{E_m} + \frac{(1-\nu_i^2)}{E_i} \qquad \textbf{(eq. 1.3)}$$

where $\nu_m$ and $E_m$ are the Poisson's ratio and the Young's Modulus for the test material, respectively. The subindex *i* denotes the values of the indenter material, where the Poisson's ratio and the Young's modulus for the diamond tip indenter are 0.07 and 1141 GPa, respectively [23].

Furthermore, the spherical tip indenter permits to construct the indentation stress-strain ($\sigma$–$\varepsilon$) curve for the material of interest using the Meyer's hardness equation:

$$\frac{P}{\pi a^2} = \frac{4}{3\pi} E_{eff} \cdot \left(\frac{a}{R}\right) \qquad \textbf{(eq. 1.4)}$$

where the left hand side of the equation represents the contact pressure ($p_m$) or the indentation stress ($\sigma$) and the ratio *a/R* is the indentation strain ($\varepsilon$).

### (b) Elasto-plastic contact: Oliver and Pharr equations

In 1992 Oliver and Pharr modified the method proposed by Doerner and Nix [17] and implemented an analysis method for directly determining the hardness (*H*) and the elastic modulus or instrumented modulus (*E*) at the same time from the indentation load-displacement curve (see **Figure 1.11)**. These properties can be determined without the necessity of imaging the residual indentation imprint [24].

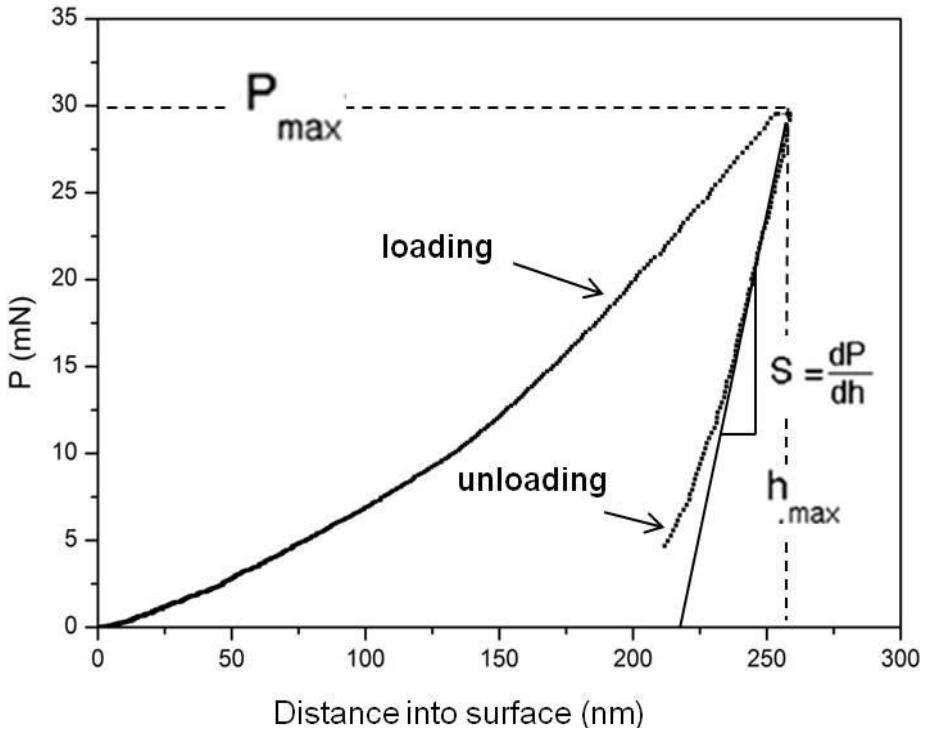


**Figure 1.11:** Load-displacement curve, where it is possible to directly extract the maximum applied load ($P_{max}$), the maximum displacement into surface ($h_{max}$) and the stiffness directly measured from the linear part in the unloading curve (S).

The exact procedure used to measure *H* and *E* is based on the unloading process, as shown schematically in **Figure 1.12**.

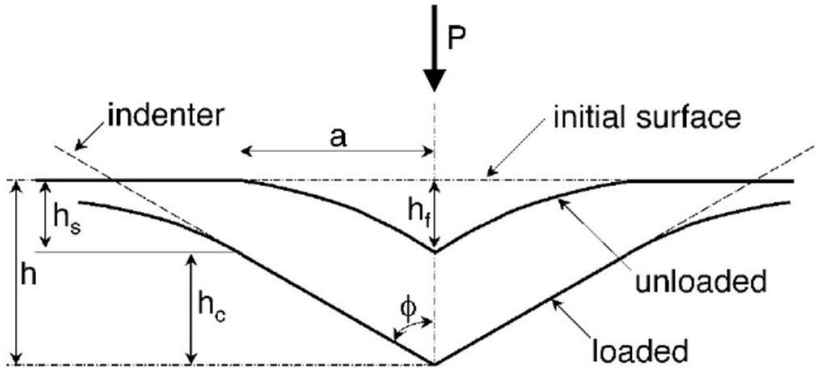


**Figure 1.12:** Schematic illustration of the unloading process [25].

Assuming that pile-up or even sink-in effects are negligible, the elastic models show that the amount of sink-in, $h_s$, can be directly determined using the following expression:

$$\mathrm{h_s} = \in \frac{\mathrm{P_{max}}}{\mathrm{S}} \qquad \textbf{(eq. 1.5)}$$

where ∈ is a constant that depends on the geometry of the indenter (about 0.75 for Berkovich indenters).

From **Figure 1.10**, the contact depth ($h_c$) can be defined using the following expression:

$$h_c = h_{max} - h_s = h_{max} - \in \frac{P_{max}}{S} \qquad \textbf{(eq. 1.6)}$$

where $h_c$ is the contact depth. The slope *S,* which can be directly determined from the unloading curve (see **Figure 1.11***),* can be expressed as follows:

$$S = \frac{dP}{dh} = \frac{2}{\sqrt{\pi}} E_{eff} \sqrt{A_c} \qquad \textbf{(eq. 1.7)}$$

where $E_{eff}$ is the effective Young's Modulus (see **equation 1.3**) and $A_c$ is the projected contact area between indenter tip and material. This parameter is estimated using the

equations for the elastic contact of an indenter of arbitrary shape on a uniform and isotropic half space, and has the following expression [17]:

$$A_c = 24.5 \cdot h_c^2 \quad \textbf{(eq. 1.8)}$$

The Berkovich tip can present some rounding effects because the shape of the indenter changes continuously (in the order of several nanometers) during the indentation process. Then, it is necessary to perfectly known the shape of the indenter tip in order to correctly determine the hardness and the elastic modulus for the specimen of interest. Thus, the area or shape function must carefully be calibrated by using Fused Silica with a well-known Young's Modulus value (72 GPa) [25]. Once the contact area is determined, the hardness can be estimated directly from:

$$H = \frac{P_{max}}{A_c} \quad \textbf{(eq. 1.9)}$$

The indentation elastic modulus and hardness for the material of study can thus be calculated without the necessity of imaging the indentation after the experiment. The hardness value derivates from the hardness measured taking into account the area of the residual impression if there is significant elastic recovery during unloading. Finally, the elastic modulus can be directly extracted using **equations 1.7** and **1.3**.

## 1.3. Sliding contact response: Nanoscratch test

The scratch test consists in generating a controlled scratch on the surface of a material, creating an elastic-plastic deformation which leads to a groove with lateral stacking, see **Figure 1.13**. This test is made for characterizing the surface mechanical properties (adhesion, fracture, deformation, among others) of thin films or coatings [26]. Given that the (ground) samples to be studied in this work, present compressive residual stresses, the surface of all the samples will be treated as a coating-like layer. A diamond tip is used for generating the scratch test. This technique permits to work using constant or

incremental loads. Incremental loads are used in plain view for evaluation of emergence of the different damage mechanisms. On the other hand, constant loads are used in cross-section for assessing possible damage mechanisms different from those evidenced in the substrate (plain view) or in the coating-like layer, i.e. to study the adhesive or cohesive damage in the interface (substrate/coating).

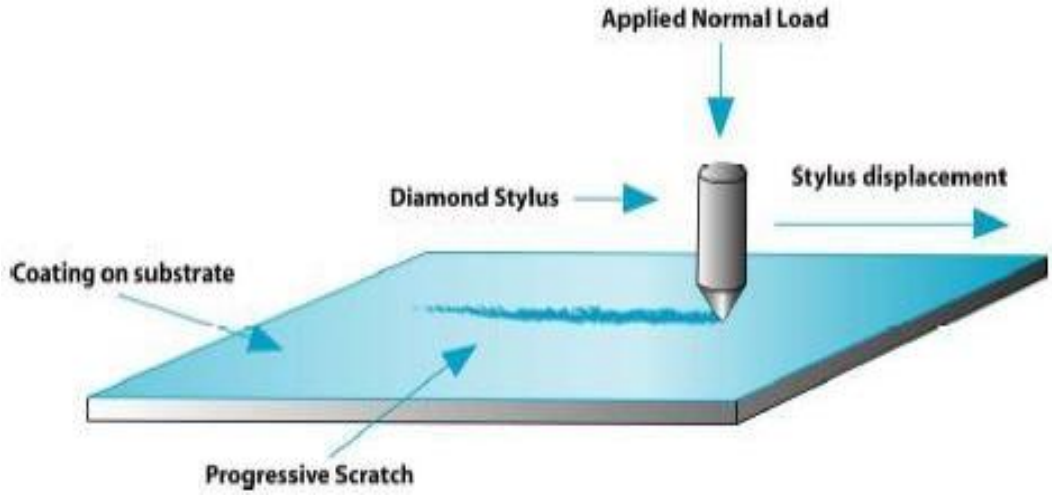


**Figure 1.13:** Scheme of a progressive scratch test [27].

Many indenters can be used during the scratch test, being the most common [28] the Berkovich and the cube corner indenter. Then, several damage and fracture events are activated inside as well as in the edge of the scratch track, like Chevron cracks and spalling, among others [29].

The nanoscratch test process can be divided in three stages: (i) original profile also known as pre-scan, (ii) scratch segment and (iii) residual profile or post-scan. **Figure 1.14** shows the results of the second stage for a nanoscratch made on ground hardmetal coated with TiN, in the longitudinal (same direction as the grinding process) and transversal direction (perpendicular to the grinding process).

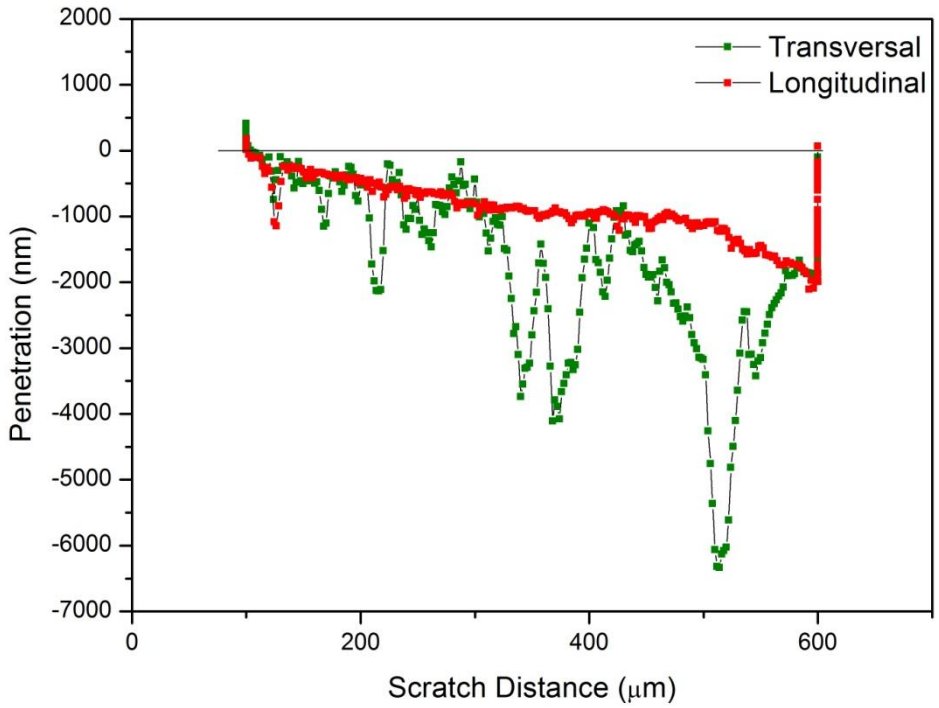


**Figure 1.14:** Nanocratch test done in the direction longitudinal and transversal to the ground.

## 1.4. Range of mechanical properties for hardmetal substrate and TiN coating.

Mechanical properties of WC-Co hardmetals are function of the properties of the constituent phases. **Table 1.2** lists the values of some mechanical properties reported in the literature for Co and WC phases contained in the hardmetal.

**Table 1.2:** Values of mechanical properties of WC and Co [30].

| | Elastic Modulus (GPa) | Poisson's' ratio | Hardness (GPa) |
|---|---|---|---|
| WC | 400-650 | 0.2-0.25 | 15-30 |
| Co | 200 | 0.31 | 2-8 |

As it has been commented in previous sections, the mechanical properties are highly dependent of the binder content and size of particles. **Table 1.3** summarizes the range of values of some mechanical properties for WC-Co composites.

**Table 1.3**: Summary of the main mechanical properties for WC-Co composite [1,31].

| Elastic Modulus (GPa) | Poisson's ratio | Compressive strength (MPa) | Hardness (GPa) | Fracture toughness ($MPa \cdot m^{1/2}$) |
|---|---|---|---|---|
| 400-600 | 0.20-0.25 | 3000-9000 | 7-25 | 5-30 |

**Table 1.4** summarizes some of the mechanical properties values for TiN reported in the literature. It can be seen that TiN has lower fracture toughness and higher hardness than WC-Co hardmetals.

**Table 1.4:** Mechanical properties for the TiN [32].

| Elastic Modulus (GPa) | Hardness (GPa) | Fracture toughness ($MPa \cdot m^{1/2}$) |
|---|---|---|
| 500-550 | 32 | 4-5 |

# 2. Objectives

The main objectives of the present study may be summarized as:

- Evaluation of grinding/polishing effects on the mechanical integrity of TiN-coated and uncoated hardmetals. In doing so, top (plain) view and cross section indentations and scratch tests were conducted at micro-and nanometric length scale. The different surface finish conditions studied were ground, polished, mirror-polished and ion etched.

- Assessment of correlations between machining-induced stresses at the surface (measured through X-Ray Diffraction) with the mechanical properties (hardness and elastic modulus) as well as with the surface finish quality. In order to reach this goal, it is necessary to study the mechanical evolution along the damages region, including the polishing speed for the WC-Co specimens.

- Proposal of an optimized protocol for mechanical characterization of surface integrity in terms of hardness and elastic modulus for specimens with residual stresses at the surface.

# 3. Experimental procedure

## 3.1. Material and surface finish conditions

The material used in this project was a fine-grained WC-13wt%Co hardmetal. It was supplied by Seco Tools [33] as prismatic bars of rectangular shapes with 4 x 4 x 53 mm dimensions. Three sets of conditions were investigated in this project: nude (AR), ion-etched (IE) and coated specimens. For each set of conditions four different surface finish variants were investigated: (1) ground (G), (2) G + thermal treatment (G+TT), (3) polished ($P_{150}$) and (4) mirror-like polished ($P_{UPC}$). All the specimens employed in this project are summarized in **Table 3.1**.

**Table 3.1:** Summary of the different specimens used in this project.

| | **G** | **G + TT** | **$P_{150}$** | **$P_{UPC}$** |
|---|---|---|---|---|
| **AR** | X | X | X | X |
| **IE** | X | - | X | X |
| **TiN COATING** | X | X | X | X |

Due to the rough abrasive machining carried out during grinding (performed by the supplier), G-samples exhibit microcracks and compressive residual stresses at the surface. G+TT specimens present same surface finish (and so microcracks), but a thermal treatment has been done over the sample aiming to relieve the existing residual stresses. $P_{150}$ samples are obtained by sequential polishing (after grinding). As result, $P_{150}$ presents little microcracks and some residual stresses, whereas in $P_{UPC}$ these features are almost negligible (as well as residual stresses, see **Figure 3.1**).

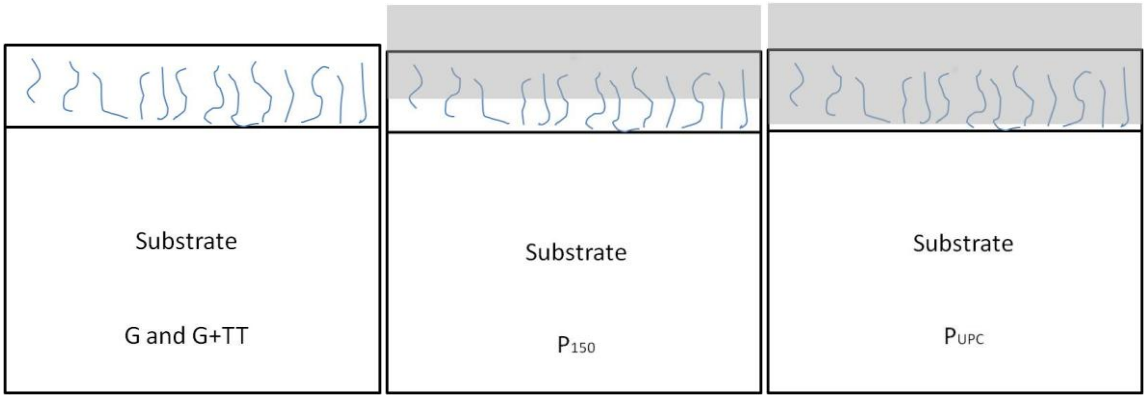


**Figure 3.1**: Scheme of microcracks in the different specimens of study.

For the mechanical characterization at micro- and nanometric length scale, two different sets of experiments were planned in order to observe how the superficial roughness affects the mechanical response: plain view and cross section experiments **(see section 4.2.1 and 4.2.2 respectively).**

## 3.2. Sample preparation

### 3.2.1. Plain view testing

All the samples where cleaned with acetone and with an ultrasonic cleaner. After that, the specimens were dried using pure air. Then, samples were mounted on an aluminum holder with a thin layer of glue.

### 3.2.2. Cross-section testing

For the cross-section experiments, specimens were cut with a Miniton cutter, from Struers (equipped with a diamond disk) in order to obtain the following dimensions for the specimens: 4 x 4 x 20 mm. Then, all the specimens were embedded in Bakelite (PolyFast from Struers). The different conditions are summarized below:

- **Heating process**: 35N during 6min at 180ºC.
- **Cooling process:** with tape water flow at 20ºC around the mounted specimen during 3 min.

The referred mounting procedure was done in order to polish the samples (obtain a flat surface) and be able to do nanoindentations in cross section to avoid any surface masking in the results. **Table 3.2** summarizes the polishing process protocol for the cross section specimens:

**Table 3.2:** Polishing process protocol for cross section specimens.

| Middle | Time (min) | Force (N) | Speed (rpm) | Polishing Disc |
|---|---|---|---|---|
| **Lubricant + diamond past 6 μm** | 20 | 15 | 150 | MD-Nap |
| **Lubricant + diamond past 3 μm** | 30 | | | |
| **Colloidal alumina suspension (20-45 nm)** | 40 | | | |

## 3.3. Mechanical characterization

### 3.2.1. Microhardness tests: Vickers Hardness

All the microindentations have been done with a microindenter (MVK-HO, Alkashi) equipped with a Vickers indenter. The load used for measuring the Vickers hardness (HV) of the specimens during this project has been kept constant and equals to 1kgf. Fifteen indentations have been done to obtain statistically reliable data.

### 3.2.2. Polishing rate

Aiming to to determine how the mechanical properties measured at the surface changes as a function of surface finish quality, it was required to evaluate the polishing rate for the studied material. This is also useful for correlating the influence of residual stresses distribution on the evaluated mechanical properties. In doing so, sequential polishing steps were made for the as received ground specimen (AR-G) in plain view.

First of all, several imprints were performed in the sample AR-G using a macroindenter (MVK HO; Alkashi) equipped with a Vickers indenter at 100 kgf of maximum applied load during 15 seconds. Before each polishing step, the lateral length of the imprint was measured by confocal laser scanning microscope (CLSM) in order to determine the

removed layer (see **Figure 3.2**). The superficial roughness evolution was also studied by using the atomic force microscopy (AFM). Finally, for each polishing state, mechanical properties were determined at different penetration depths, (250 and 2000 nm) in order to observe how sensitive the nanoindentation technique is to the existing superficial roughness.

Since the shape of a Vickers indenter is perfectly known, the depth of the indents can be directly determined from the measurement of the lateral size of the surface square associated with the indent. For a Vickers indenter, the area of a section perpendicular to the indenter axis is given by:

$$\mathrm{A} = 24.5 \cdot \mathrm{h}^2 \qquad \textbf{(eq. 3.1)}$$

where *h* is the height of the section relative to the apex of the indenter. As the indenter is often blunt, a tip defect ($h_o$) should be taken into account, then the previous equation can be modified as follows:

$$A = 24.5 \cdot (hp + ho)^2 \qquad \textbf{(eq. 3.2)}$$

where $h_p$ is the residual depth of the indent The projected area *A* of a Vickers indent can also be determined from direct observation of the residual indent as:

$$A = l^2 \qquad \textbf{(eq. 3.3)}$$

where *l* is the lateral length of the imprint. Combining **equations 3.2** and **3.3**, the thickness $\Delta h$ of the removed layer between two successive polishing steps can be expressed as follows:

$$\Delta h = h_{p,1} - h_{p,2} = \sqrt{\frac{A_1}{24.5}} - \sqrt{\frac{A_2}{24.5}} = \frac{l_1 - l_2}{4.95} \qquad \textbf{(eq. 3.4)}$$

where $l_1$ and $l_2$ are the lateral sides of the residual indenter after two successive polishing stages (see **Figure 3.2**).

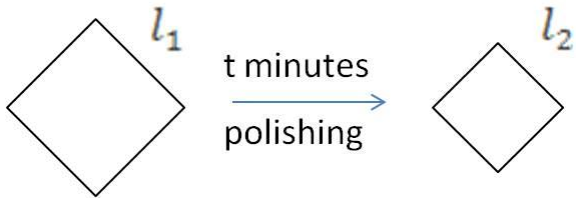


**Figure 3.2:** Determination of the polishing rate from the lateral size of the microindents.

## 3.4. Instrumented indentation

Assessment of local mechanical properties at the surface layer included the evaluation of their effective hardness (*H*) and indentation Elastic modulus (*E*) through instrumented indentation technique (IIT). It was performed using a nanoindenter XP (MTS) equipped with a continuous stiffness measurement (CSM) module, the latter allowing a dynamic determination of hardness and elastic modulus during the indentation [17]. The strain rate during the indentation process was held constant at 0.05 $s^{-1}$. The indenter shape was carefully calibrated for penetration depths as small as 100 nm by indenting fused silica samples of accurately known Young's modulus (72 GPa). The values of hardness and elastic modulus were calculated by the Oliver and Pharr method [23] assuming a constant Poisson's ration for the specimens of study equals to 0.25. Using this technique, three different sets of experiments were done:

(i) **Plain view measurements** with different surfaces finish qualities at 2000 nm of maximum penetration depth (or until reaching the maximum applied load of the equipment, 650 mN). The imprints were distributed in a homogeneous array of 36 imprints (6 by 6), with a constant distance between imprints of 50 μm in order to avoid any overlapping effect, (**Figure 3.3a)**.

(ii) **Evolution of plain view measurements** as G-surface layer was sequentially removed (and surface roughness was consequently diminished). Homogeneous array of 16 experiments (4 x 4) at 250 nm and 2000 nm of maximum penetration depth with a

constant distance between imprints of 20 μm and 50 μm respectively (in order to avoid any overlapping effect).

(iii) **Cross section measurements**, from the region free of damage for the WC-Co grade of study until the surface-like region of interest (with microcracks and with compressive residual stresses, (see section 3.1 and **Figure 3.3b**). This process consists in performing a line of regularly spaced indentations. The accuracy of the measurements is strongly related to the size of the indents. They must be small enough to probe a small volume and thus to obtain a good spatial resolution, but also to avoid artifacts when the indents are close to the interface between the sample and the Bakelite. For this reason, all the indentations have been performed in displacement controlled mode. The penetration depth was increased linearly until reaching 250 nm with a constant spacing distance of 5 μm to avoid any overlapping effect. Furthermore, three imprints per line have been realized in order to perform an statistical analytics. In this way, in the hardness vs. distance profile, each point is averaged over three different measurements.

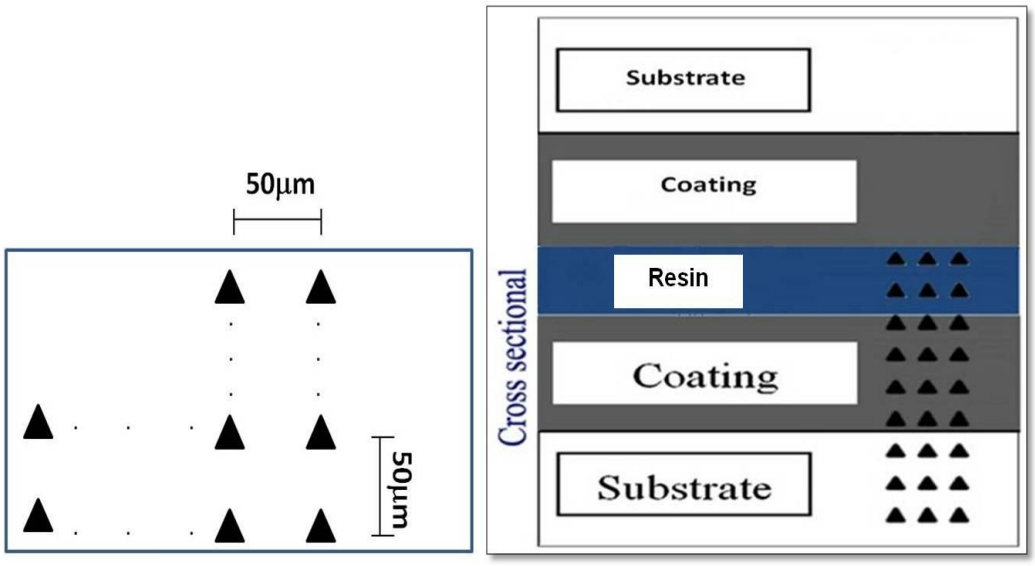


**Figure 3.3:** Indentation scheme of **(a)** Plain view and **(b)** cross section [34].

## 3.5. Nanoscratch testing

Nanoscratch tests were performed using a Nanoindenter XP System from MTS with a load control mode. For this study a Berkovich indenter was used with the indenter pointing with one of its corners in the scratch direction. Samples were oriented such that nanoscratch directions were aligned longitudinal or transversal to grinding direction. In order to induce several cracks along the sliding track, a Berkovich indenter was used.

Tests can be done at constant or increasing load. In order to determinate when the different damage mechanisms emerge, an increasing load was applied (**Figure 3.4**). It increased along the scratch from 0 mN to 500 mN (after 500 μm sliding contact). The tip velocity was held constant to 10 μm/min. For the AR samples (mainly G and G+TT) nanoscratch tests were done pararel and perpendicular to the grinding lines.

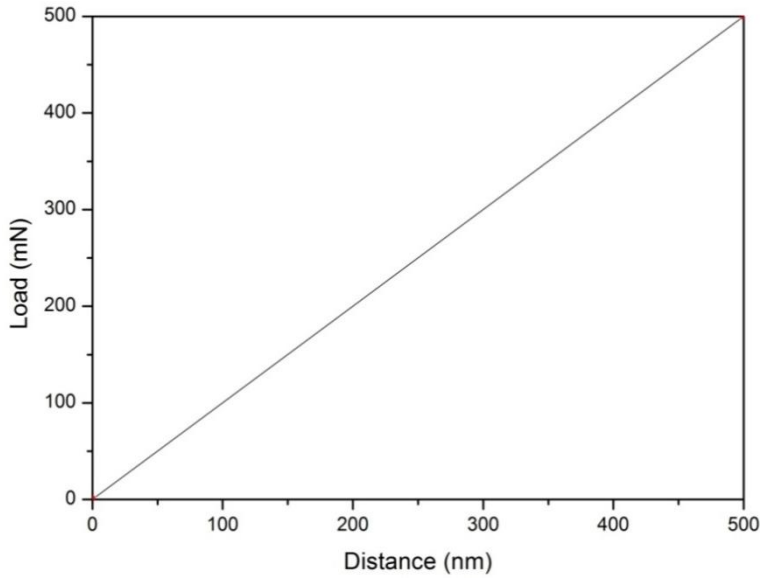


**Figure 3.4:** Representation of the imposed load in function of the distance.

# 3.6. Surface characterization

## 3.6.1. Laser scanning confocal microscope, LSCM

A laser scanning confocal microscopy (LSCM) is an optic microscopy that can produce images at low depth of field. With the LSCM it is possible to produce a set of images from which a three-dimensional (3D) representation of the sample may be obtained.

The light emitted by the laser system (excitation source) passes through a pinhole aperture that is located in a conjugate plane (confocal) with a scanning point on the specimen and a second pinhole aperture positioned in front of the detector (a photomultiplier tube), (**Figure 3.5)**.

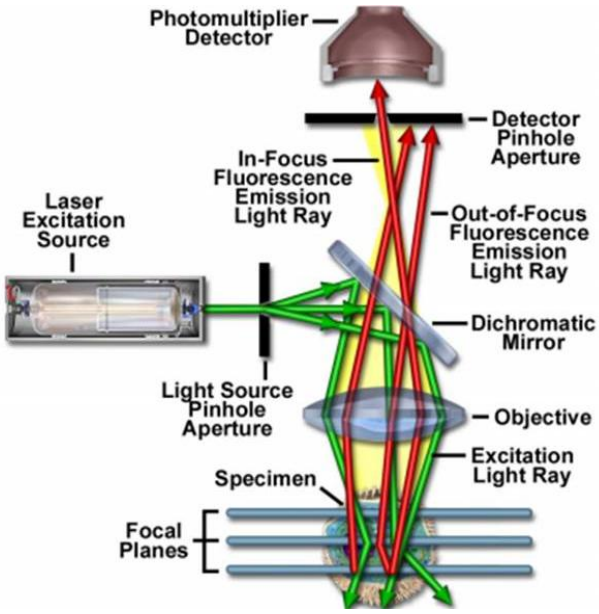


**Figure 3.5**: Schematic diagram of the laser scanning confocal microscope [35].

As the laser is reflected by a dichromatic mirror and scanned across the specimen in a defined focal plane, secondary fluorescence emitted from points on the specimen (in the same focal plane) passes back through the dichromatic mirror and is focused as a confocal point at the detector pinhole aperture.

In this study an OLYMPUS-LEXT OLS Confocal microscope was used.

### 3.6.2. Field emission scanning electron microscopy, FESEM

The field emission scanning electron microscopy (FESEM) is a type of electron microscope that images the sample surface by scanning it with a high-energy electron beam. A field-emission cathode in the electron gun liberates electrons which, accelerated in a high electrical field gradient, enter the surface of a sample and generate low energy secondary electrons, (**Figure 3.6)**.

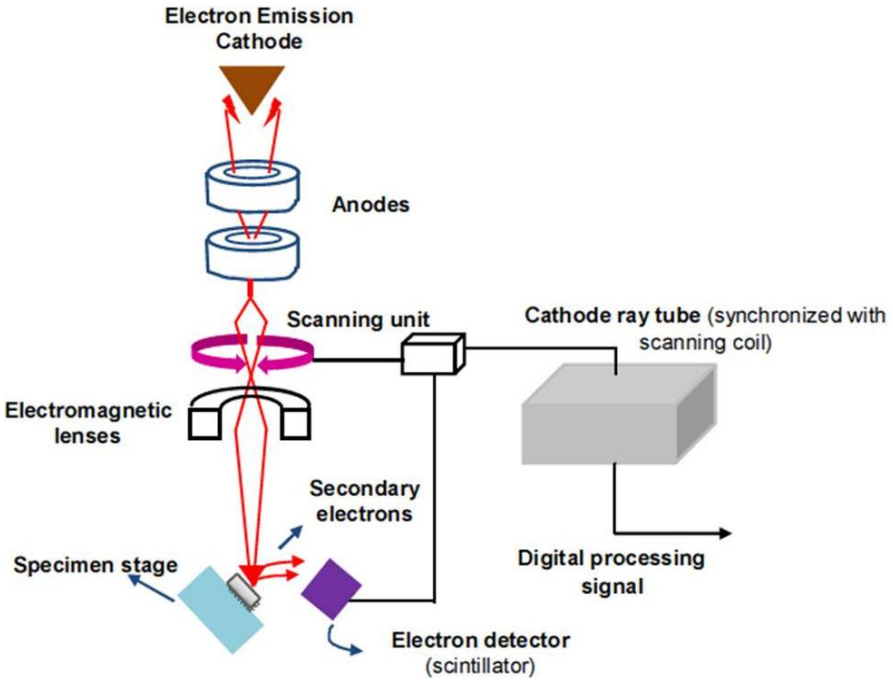


**Figure 3.6:** Field emission scanning electron microscopy scheme [36].

The intensity of these secondary electrons depends on the topography of the sample. An electron detector called the “scientillator” catches these secondary electrons and produces an electronic signal (and then an image of the sample surface) by measuring its intensity as function of the position of the scanning primary electron beam.

The equipment used in this project to observe the superficial damage generated by microindentation, nanoindentation as well as nanoscratch was a Jeol JSM-7001F–FESEM.

### 3.6.3. Atomic force microscopy, AFM

The Atomic Force Microscopy (AFM) is a very high resolution scanning probe microscope in *z*-axis. There are two main modes of operation for the AFM: static (continuous, also known as contact mode) or dynamic (oscillating, also known as tapping mode). In the static mode the tip is constantly in contact with the surface, whereas in the dynamic mode the tip oscillates on a determined frequency by tapping the surface. In this project, all the AFM scans were done in tapping mode.

AFM in tapping mode works by scanning a tip over the sample to sense the topography of the surface, producing a three dimensional images of the sample surface with nanoscale resolution at the same time: error, phase and topographic images. When the sample and tip come into proximity, the cantilever is deflected due to the forces between the sample and the tip. The deflection is usually measured using a laser reflected on the top of the surface of the cantilever into an array of photodiodes [37], (**Figure 3.7)**.

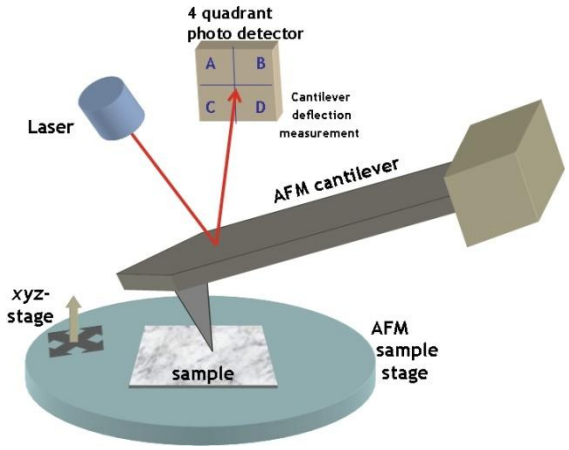


**Figure 3.7:** Atomic force microscopy scheme [37].

AFM images were obtained by an AFM Dimension 3100 from Bruker and were subsequently analyzed using the WSxM 5.0 software [38].

# 4. Results and discussion

## 4.1. Residual stresses at the surface, as induced by grinding

Grinding induces compressive residual stresses at the surface level, as it has been measured by XRD diffraction in Linköpink University and supplied by Yang [39]. **Figure 4.1** shows a histogram representing the compression stresses at the surface of the studied specimens.

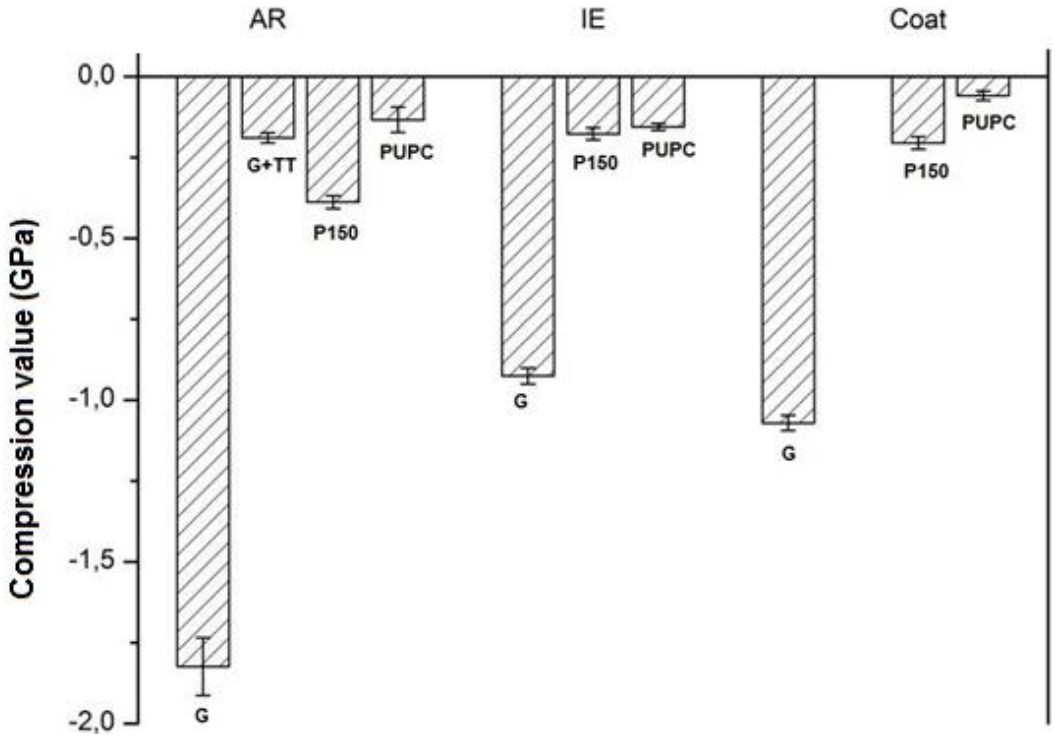


**Figure 4.1:** Representation of the compression stress value of the specimens [39].

By doing the heat treatment, it may be seen that the compressive residual stresses are relieved. In all the cases the highest value is for G-specimens. $P_{150}$ exhibit low compression stress values. Compressive stress value decreases with Ion Etch treatment, and it does not change after TiN coating.

Likewise, compression stress values of the sample AR-G have been measured and represented as a function of depth from the surface (**Figure 4.2**). Considering that there are compression stresses distributed in a ~15μm surface layer, it will be treated as a

coating-like layer. Also, this graph clearly shows that the damage layer presents a thickness of about 12 μm, yielding a base line compression stresses at that point of around – 250 MPa.

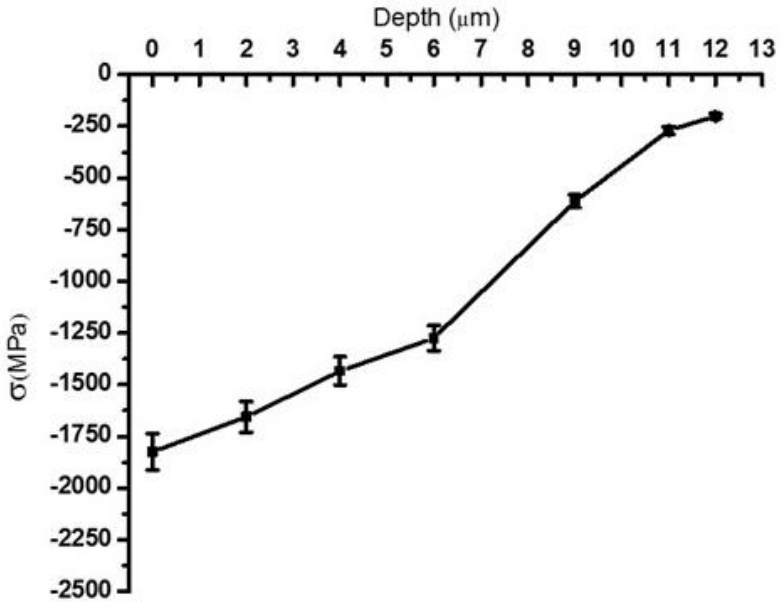


**Figure 4.2:** Representation of compression stress as a function of depth for the AR-G sample [39].

## 4.2. Mechanical properties:

### 4.2.1. Plain view

#### 4.2.1.1. Microindentation

The results concerning the hardness obtained with Vickers' indentation test for all the conditions studied on this project are shown in **Figure 4.3**. In all the cases the highest hardness value (*HV*) is found for the ground sample, given that compression stress oppose to the applied load. Likewise, it can be seen that for the same surface quality finish (ground), after doing a thermal treatment *HV* decreases (given that the compressive stresses are somehow relieved).

In the AR-group *HV* decreases by 18% with the thermal treatment whereas *HV* for specimens G+TT, $P_{150}$ and $P_{UPC}$ is almost the same. So, microcracks do not influence too much hardness, pointing out compression stresses as key factor in microhardness assessment.

In the case of the group with the IE treatment, G presents a slightly higher hardness value than $P_{150}$ and $P_{UPC}$, which have almost similar level (1600 HV).

Finally, in the case of the Coat-group, G, $P_{150}$ and $P_{UPC}$ have almost the same *HV*, whereas G+TT has a hardness 10% lower than G. TiN is harder than WC-Co as it has been reported and summarized in the a previous section (see section 1.4 and Table 1.3 and 1.4 for WC-Co substrate and TiN coating respectively. This could explain the relatively higher HV hardness values of the coat-ground as compared to AR and IE ones, particularly for $P_{150}$ and $P_{UPC}$ specimens, where damage features and compressive residual stresses have been somehow removed during polishing (**Figure 4.4**)

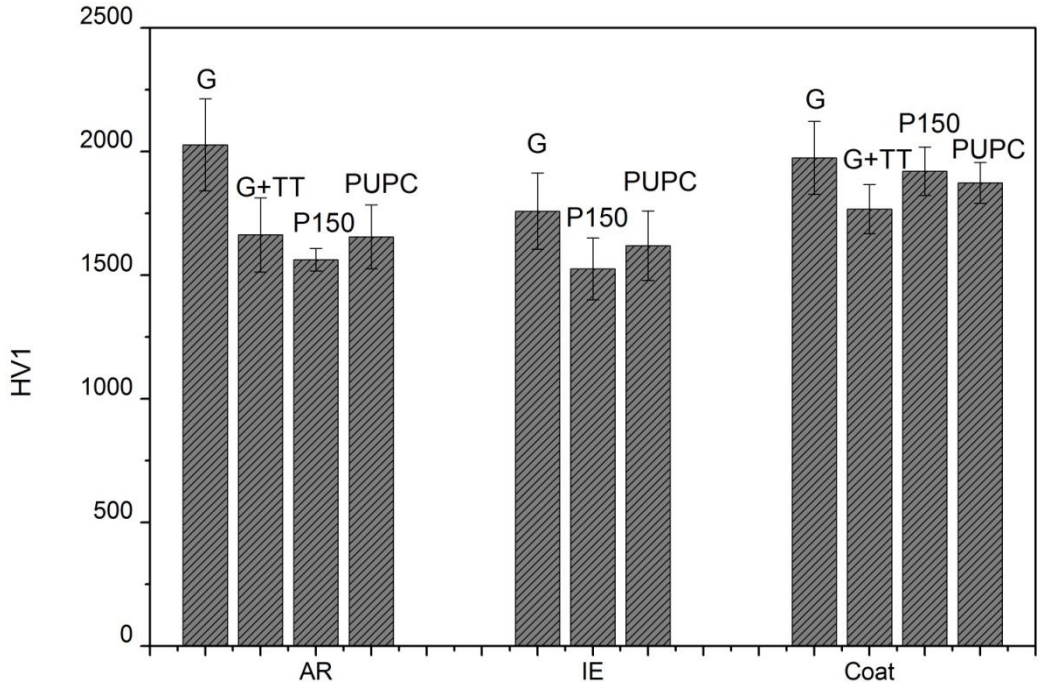


**Figure 4.3:** Representation of the Hardness measured with Vickers' indentation at 1 kgf.

The similar hardness value measured for AR-G and Coat-G should be a compromise from the relatively lower residual stresses (IE-G vs. AR-G) and the hardness increase provided by the hard coating layer (Coat-G vs. IE-G).

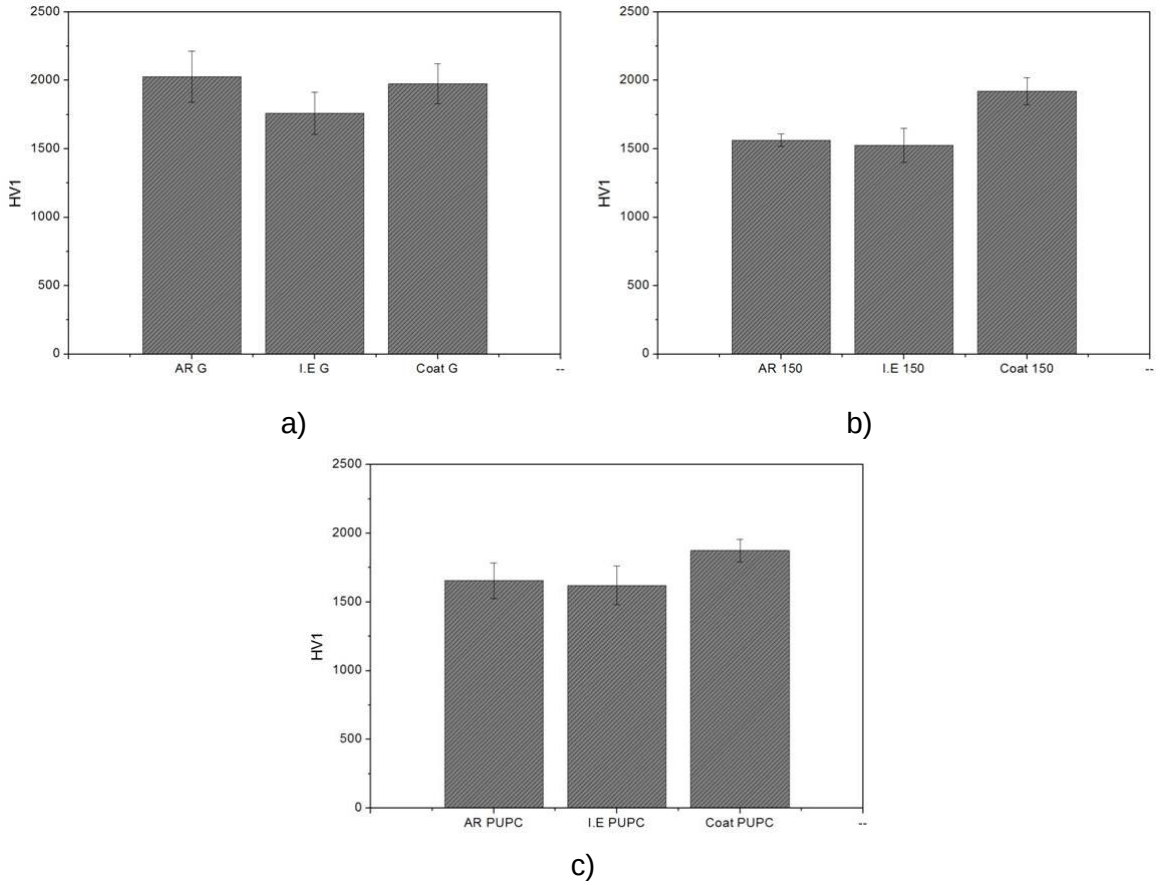


**Figure 4.4:** Representation of the Hardness measured with Vickers' indentation for the different samples.

In **Figure 4.5** HV1 values are plotted against measured residual stresses for all the studied specimens. It is clear that lower hardness values determined for G-IE comes from removal of surface layer where compressive stresses where distributed. This is not the case for P specimens as main surface charges have already induced during polishing. On the other hand, coating promotes increasing hardness for all IE conditions, resulting in a similar hardness value (for the G specimen) to those measured for AR-G.

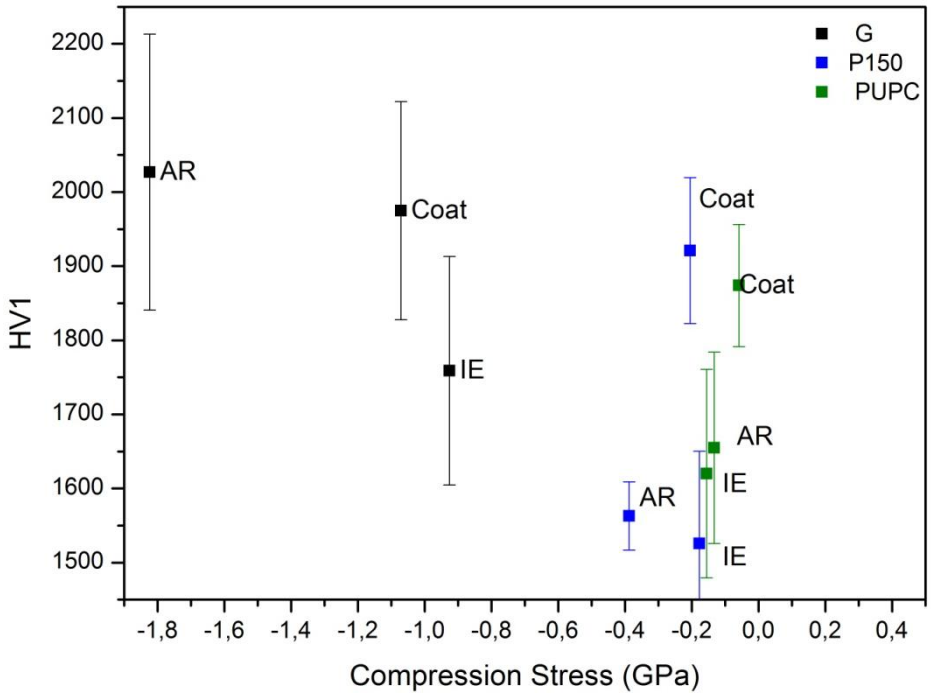


**Figure 4.5**: Representation of H as function the compression stresses.

Indentations made on the specimens have been observed with a FESEM in order to study if they had induced damage in the material as well as to observe the shape of the residual imprint. It will give information about possible surface quality (roughness) effects. The images for the different residual Vickers' imprints are shown in **Figure 4.6**. Left hand side presents the general view of the Vickers' imprint, while the right hand side exhibits a magnification of one side of the imprint, in order to show several damage mechanisms induced during indentation.

As it can be observed in **Figure 4.6**, there is a crack at the end of the diagonal in the case of the AR G+TT, but it is not appreciated in G. The heat treatment made on the sample is the responsible of crack emergence in G+TT, because all the compressive stresses have been removed. Furthermore, microcracks cannot be evidenced in the AR-G specimen because the superficial roughness mask the different damage features activated during the indentation. In the case of $P_{150}$ and $P_{UPC}$, some damage may be discerned. For the $P_{UPC}$ specimen one can observe a microcrack at the corner of the residual imprint, effect may caused by some decohesion between particles when indenting the material of interest.

Regarding indentation geometry, it may be observed that in the case of G and G+TT, the impression geometry is far from the ideal indenter's geometry (a square shape). The cause of this different geometry is the samples' roughness. Even if for $P_{150}$ and $P_{UPC}$ one neither have the same geometry or indenter area, it is not so different as in the case of G and G+TT, see **Figure 4.6**. Indentations imprints for the specimens G and G+TT present a high scatter because of the surface roughness. Likely, microhardness and nanohardness values (that will be presented in the oncoming section) exhibit a high scatter for specimens G and G+TT, especially AR-samples.

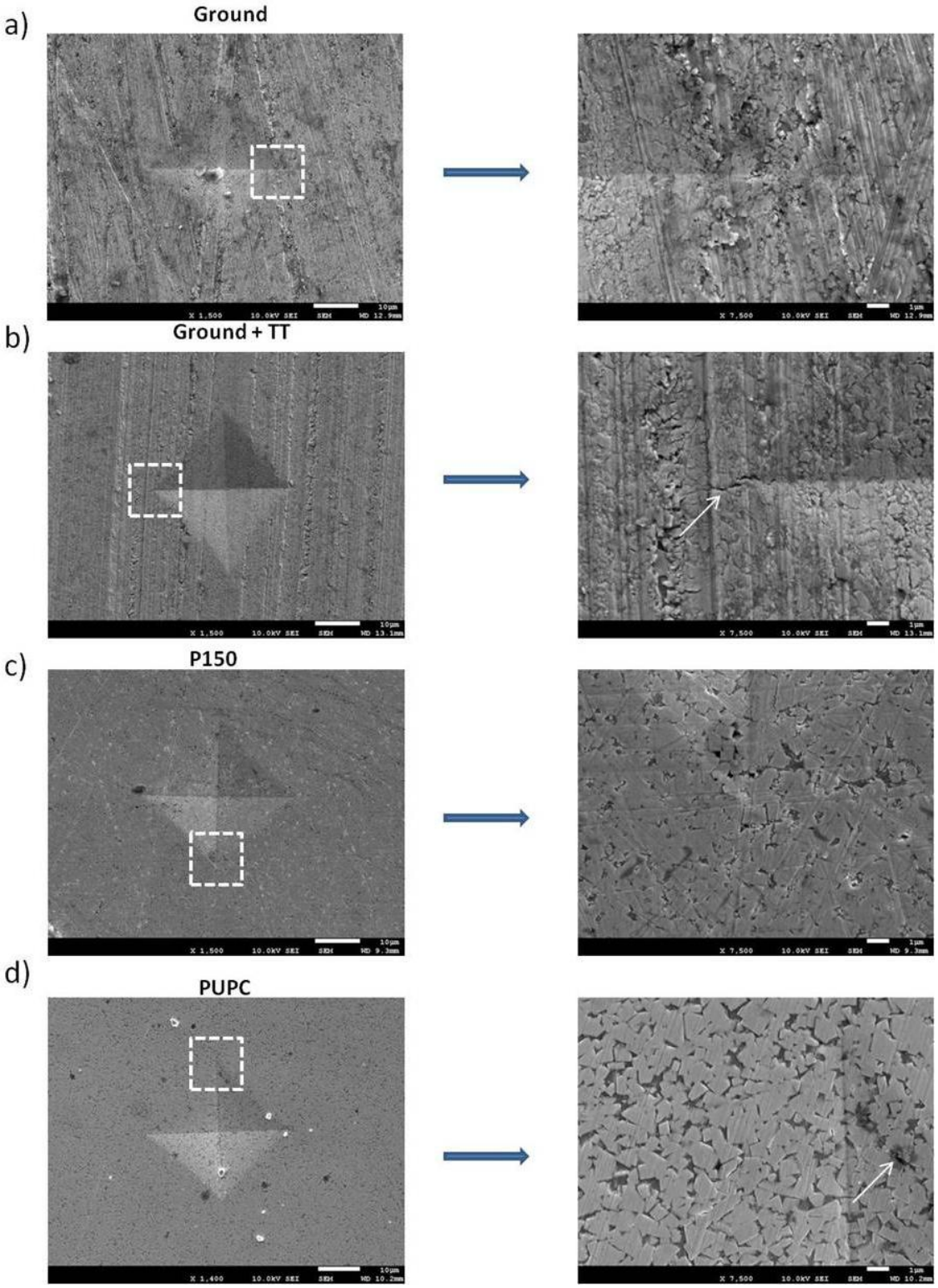


**Figure 4.6**: Vickers' impression image of AR-samples taken with the FESEM. (a) G, (b) G+TT, (c) $P_{150}$, and (d) $P_{UPC}$.

**Figure 4.7** shows some of the indentations done on Ion Etch specimens for the G and $P_{UPC}$ samples. The $P_{150}$ images are not shown in this report because these images do not provide any additional information. In this image, the left hand side presents general views of the Vickers' imprint, while the right hand side shows a magnification of one side of the imprint in order to observe the activation of several damage events induced during indentation.

It may be seen that G do not present any crack whereas $P_{UPC}$ presents a little crack at the end of one of the diagonals. The strain field induced by the indenter is confined near to the residual imprint. As the damaged layer (compressive stresses and/or microcracks) is removed, it could be expected one could expect to find easily the cracks induced by the indentation, as one can appreciate in **Figure 4.7** and furher in **Figure 4.27**. However, as it can be appreciated in the right hand side image, the roughness generated by the IE treatment can mask the observation of damage mechanisms around the residual imprint.

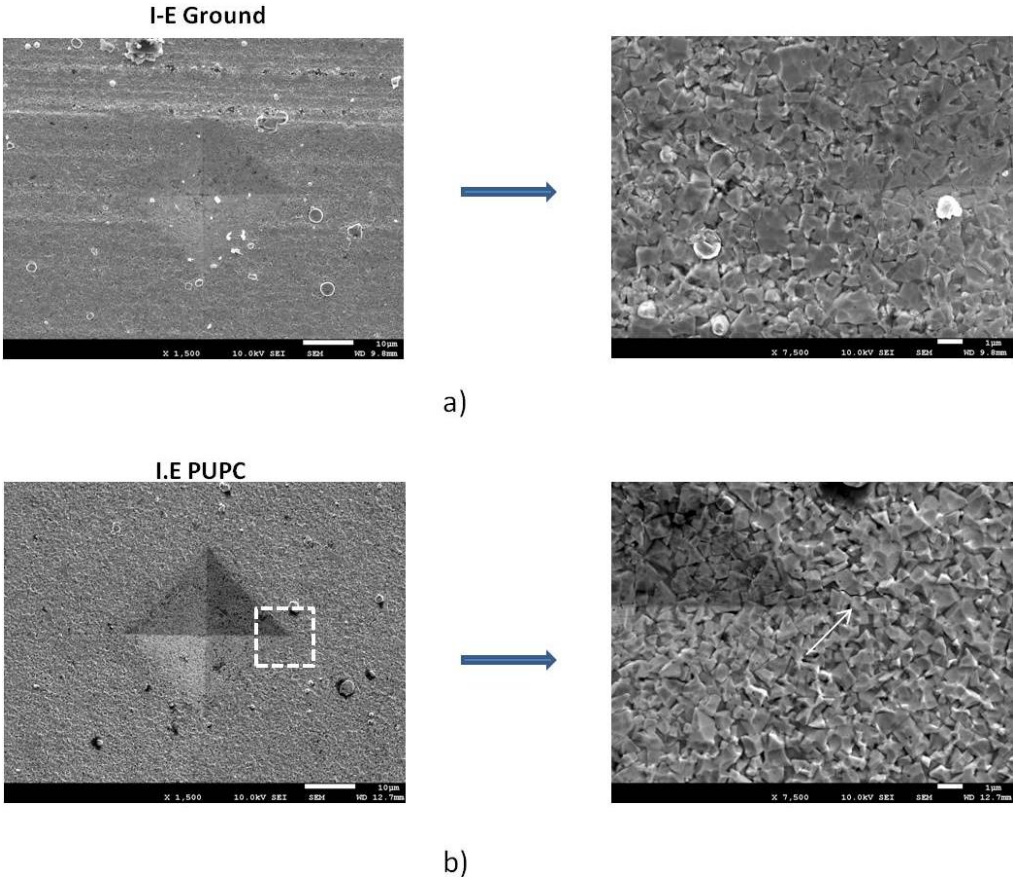


**Figure 4.7**: FESEM Vickers' impression image of IE-samples. (a) G, and (b) $P_{UPC}$.

Finally, the indentations done on the specimens with TiN coating have also been observed with the FESEM (**Figure 4.8**). In that case, the superficial observation points out that the TiN coating is highly heterogeneous due to the presence of high amount of drops deposited during the deposition process. These drops can slightly change the fracture events induced during indentation process. Unlike the other cases, in **Figure 4.8** it can be seen that all the specimens present cracks in (at least) one of the edges of the corners of the residual imprint. This effect should be attributed to the lower fracture toughness of TiN with respect to WC-Co.

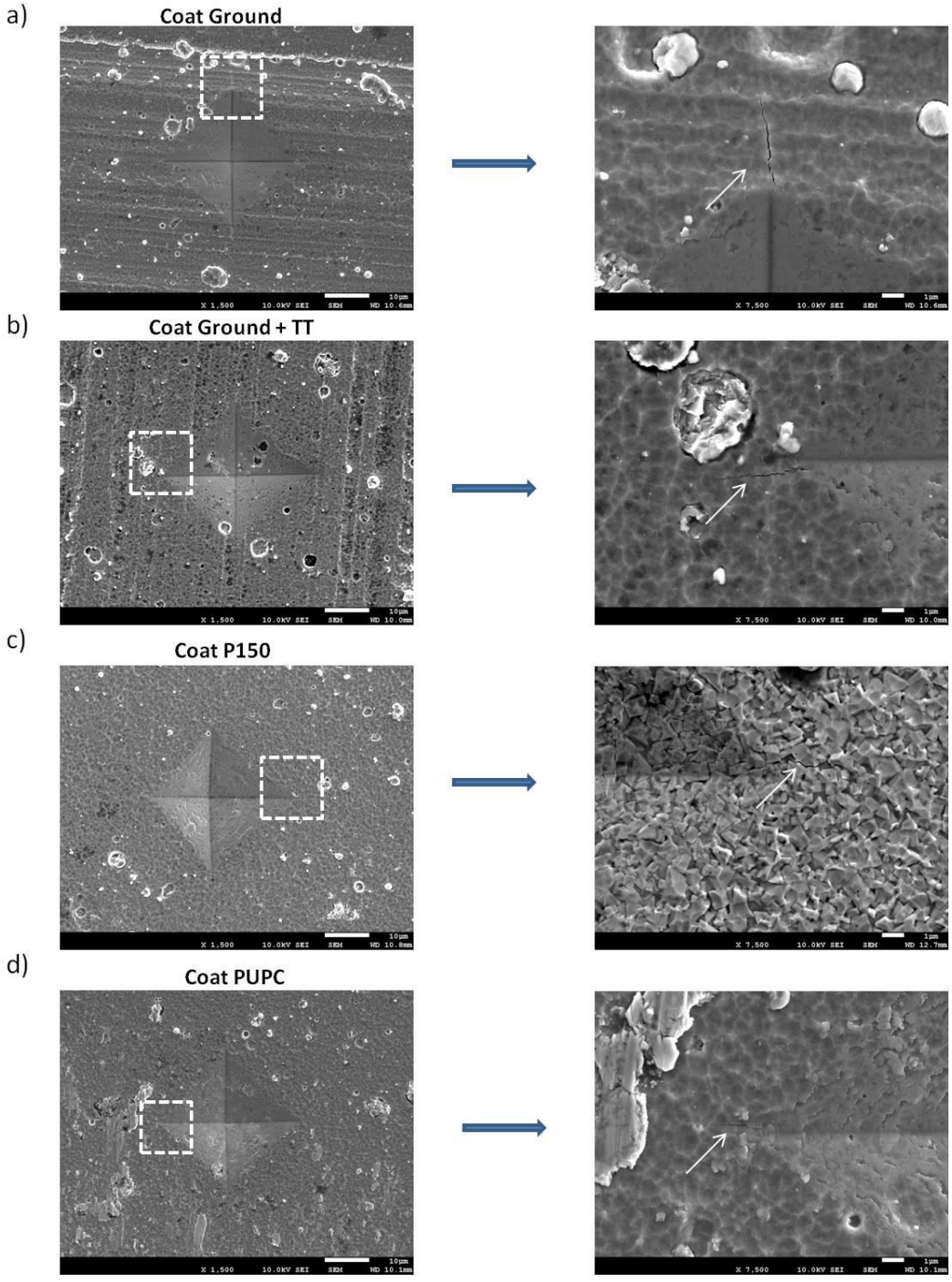


**Figure 4.8:** FESEM image of several residual Vickers' Impression of Coating-samples. (a) G, and (b) $P_{UPC}$.

As it can be seen in **Figure 4.3** and **Figures 4.6** to **4.8**, Vickers' indentations do not provide detailed information: one can observe some difference in the hardness values measured (in plain view) between the G and the other samples, but there is not any clear

evidence given that the indentation imprint is too big and the residual indentation interacts with the material free of defects. Hence, in order to avoid this interaction, nanoindentations test were done with 2000 nm as maximum indentation depth.

#### 4.2.1.2. Nanoindentation

Hardness and elastic modulus measured with the nanoindentation test have been evaluated and represented as a function of the displacement into surface in **Figure 4.9**. Two different regions may be observed: one at penetration depths lower than 300 nm, where the residual stresses and the superficial damage modifies the mechanical properties; and another for displacements into surface higher than 300 nm, where the mechanical properties remains constant.

Several observations may be indicated. First, (**Figure 4.9a**) one can observe (as it has been said before) the two different tendencies. One from 0 to 300 nm and the other from 300 nm until the end, where the mechanical properties remains constant. From left to right: for little penetration depth, $P_{150}$ has the higher hardness value (*H*) and G the lowest one. Likely, $P_{150}$ has the highest elastic modulus value (*E*) and G the lowest one. G+TT, $P_{150}$ and $P_{UPC}$ reach quickly a high value of *H* and *E*, whereas G takes more time maybe affected by the compressive stresses layer. With increasing the distance into the surface, the value of hardness for all the samples tend to be the same (around 20 GPa) except for the G+TT that is slightly lower (17.5 GPa) than the others. However, this change is not significant due to the large scattering associated with each mechanical value. The elastic modulus value is around 500-550 GPa for the four samples. These values of *H* and *E* are in correct agreement with different works published in the literature and summarized in **section 1.4**.

In the case of samples with Ion Etch treatment (**Figure 4.9b**), the trends above described are also present. For penetrations' depths under 300 nm, G is the hardest sample and $P_{150}$ and $P_{UPC}$ have the same *H*. Moreover, the hardness at low surface's distance is slightly higher than the *H* penetrations distances higher than 300 nm. For high penetrations depths G has a hardness value around 20 GPa and $P_{150}$ and $P_{UPC}$ have the same hardness (around 18 GPa). What concern to the elastic modulus values, for penetrations depths under 300 nm there is an important difference between G and $P_{150}$ and $P_{UPC}$, which have the same value. For high penetrations depths, the elastic modulus

of G decreases with the penetration distance (probably due to microcrack present on the sample) especially for distances to the surface between 300 and 600nm. $P_{UPC}$ presents a slightly higher value than G and P150.

Finally, in the case of the coated samples with TiN (**Figure 4.8c**), one can appreciate that the $P_{UPC}$ has the highest hardness value (30 GPa), having G and $P_{150}$ samples a hardness value of 24 GPa (it has increased because TiN is harder than WC-Co). However, these range of hardness (24-30 GPa) is in agreement with the TiN hardness reported in the literature, see **section 1.4**.

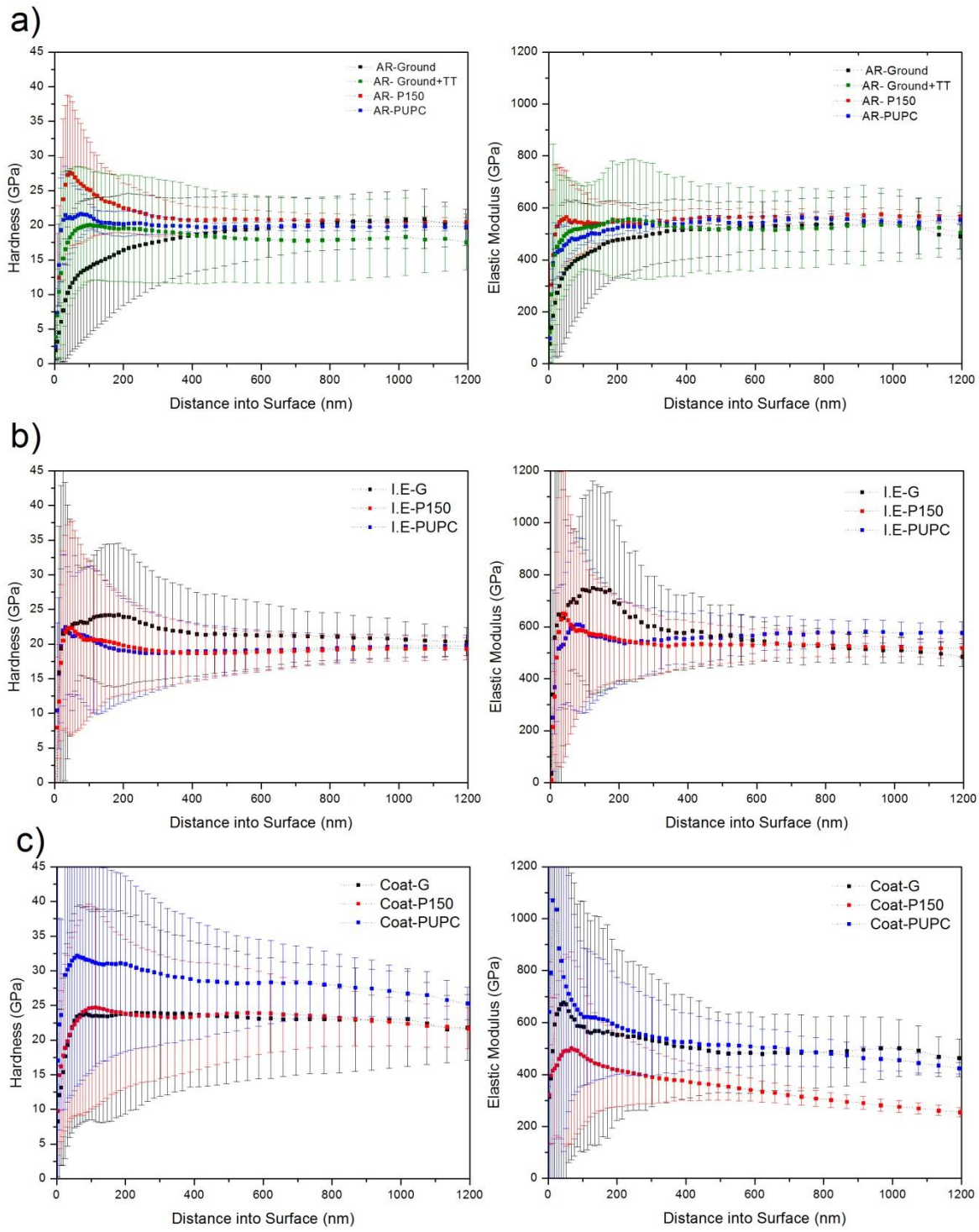


**Figure 4.9:** Representation of Hardness (H) and elastic modulus (E) in function of the distance into the surface for the different specimens of study. (a) AR, (b) IE, and (c) Coated.

Hardness and Elastic modulus values of all the samples are summarize in **Table 4.1** and **Table 4.2** respectively, for a constant penetration depth of 1000 nm. One can observe that

the hardness for the AR and In Etch specimens presents the same hardness value, reaching the hardest one when the specimens are coated with TiN due to the latter being harder than the WC-Co. Moreover, for AR and IE samples, all the specimens have same hardness value (around 20 GPa). In the case of the coating, $P_{UPC}$ has a higher value (26.7 GPa).

**Table 4.1:** Resume of hardness value at 1000 nm measured with the nanoindenter (in GPa).

| | G | G+TT | P150 | PUPC |
|---|---|---|---|---|
| **AR** | 20.8 ± 4.2 | 18.5 ± 5.5 | 20.1 ± 0.7 | 19.9 ± 0.7 |
| **IE** | 20.7 ± 2.6 | - | 19.3 ± 1.8 | 19.7 ± 1.6 |
| **TiN coating** | 23.0 ± 6.9 | - | 22.4 ± 3.3 | 26.7 ± 3.5 |

**Table 4.2:** Resume of Elastic modulus value at 1000 nm measured with the nanoindenter (in GPa).

| | G | G+TT | P150 | PUPC |
|---|---|---|---|---|
| **AR** | 537 ± 169 | 532 ± 138 | 568 ± 25 | 544 ± 10 |
| **IE** | 510 ± 49 | - | 521 ± 36 | 573 ± 44 |
| **TiN coating** | 502 ± 109 | - | 276 ± 27 | 456 ± 43 |

As we appreciated for the microhardness test, the surface quality can mask and modify as well as to observe some sink-in or pile-up effect surrounding the residual imprint for the mechanical properties performed in plain view. For that reason, all the different residual imprints for the different specimens of study have been observed by AFM (see **Figure 4.10)**.

In **Figure 4.10** one do not observe any fracture mechanism. G and G+TT samples (as occurred in Vickers' indentation) do not present a perfect Berkovich indentation due to the surface roughness, and that's why the hardness and elastic modulus values had a scatter as high as it is reported in **Figure 4.9**.

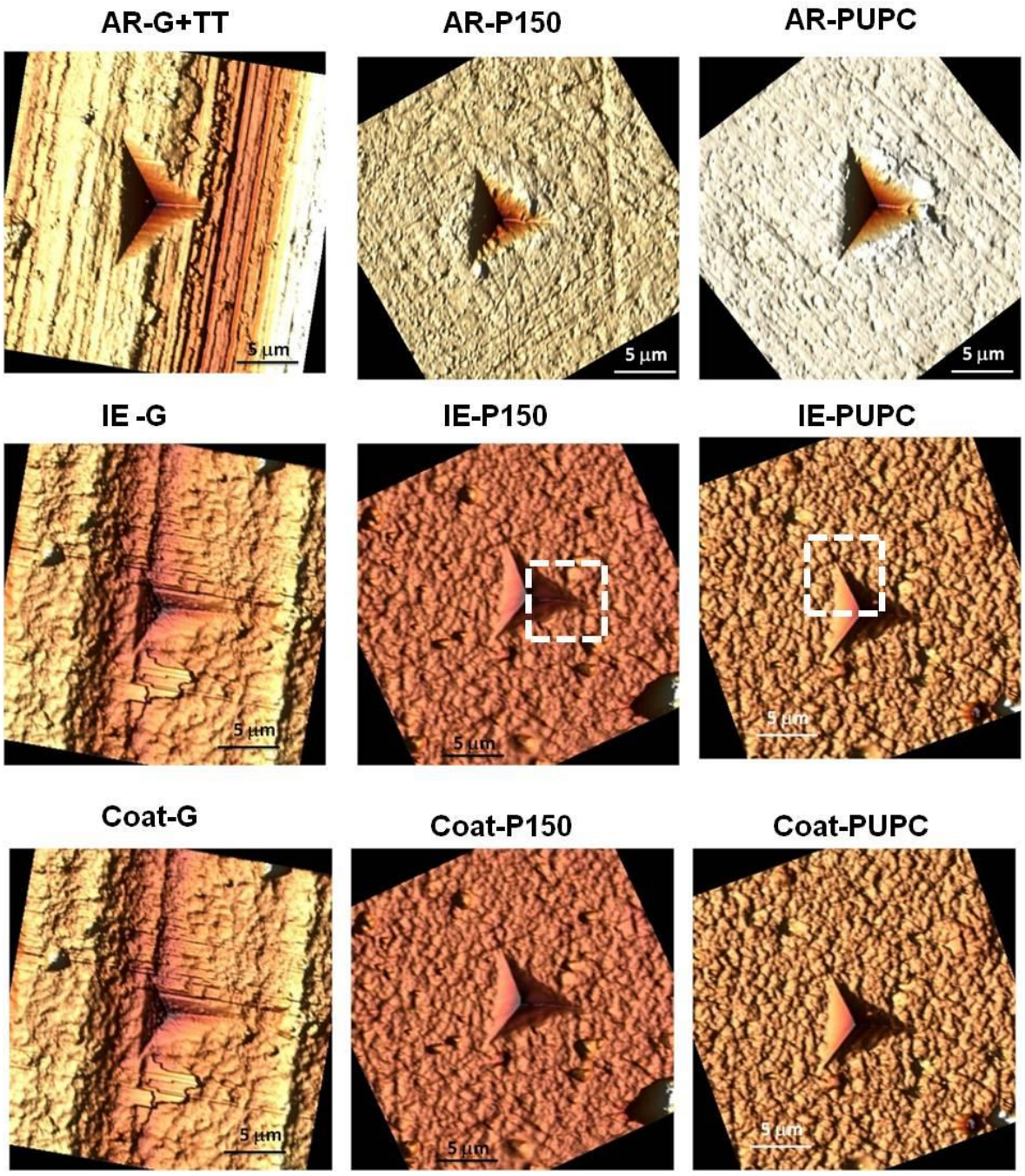


**Figure 4.10**: AFM images (3D view, 25 x 25 $\mu m^2$) of Berkovich indentations. All the samples were observed with AFM but here are not all presented because no supply additional information.

A detail of the samples IE-$P_{150}$ and IE-$P_{UPC}$ is shown in **Figure 4.11.** One can see that there is any crack or any damage mechanism surrounding the residual imprint.

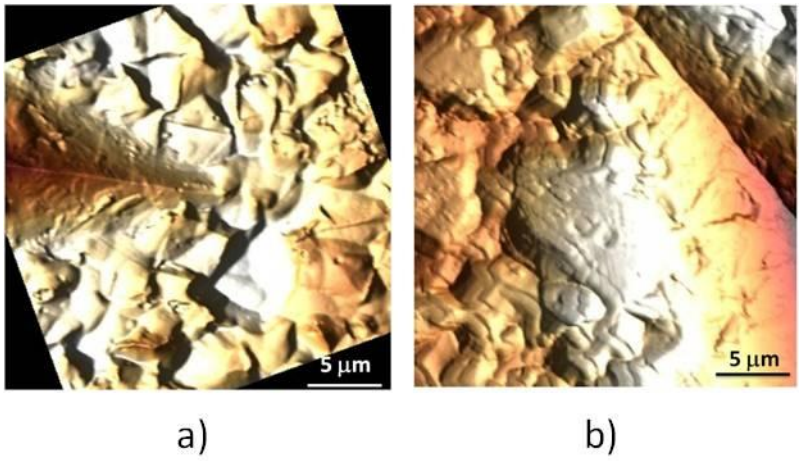


**Figure 4.11**: AFM (3D view, 25 x 25 μm$^2$) detail of IE-P150 (a) and IE-PUPC (b)

Surface roughness also affects the accuracy of the determination of the mechanical properties at micrometric length scale as illustrated in **Figure 4.12**. Because of surface roughness one cannot prove any pile-up effect in the case of AR-G+TT, whereas in the AR-$P_{150}$ profile one can see some uprising on the right hand of the indentation. This effect can be attributed to the superficial roughness for the specimen of study. In summary, this figure gives information that the shape of the residual imprint is strongly modified by the roughness as it can be appreciated in this profile.

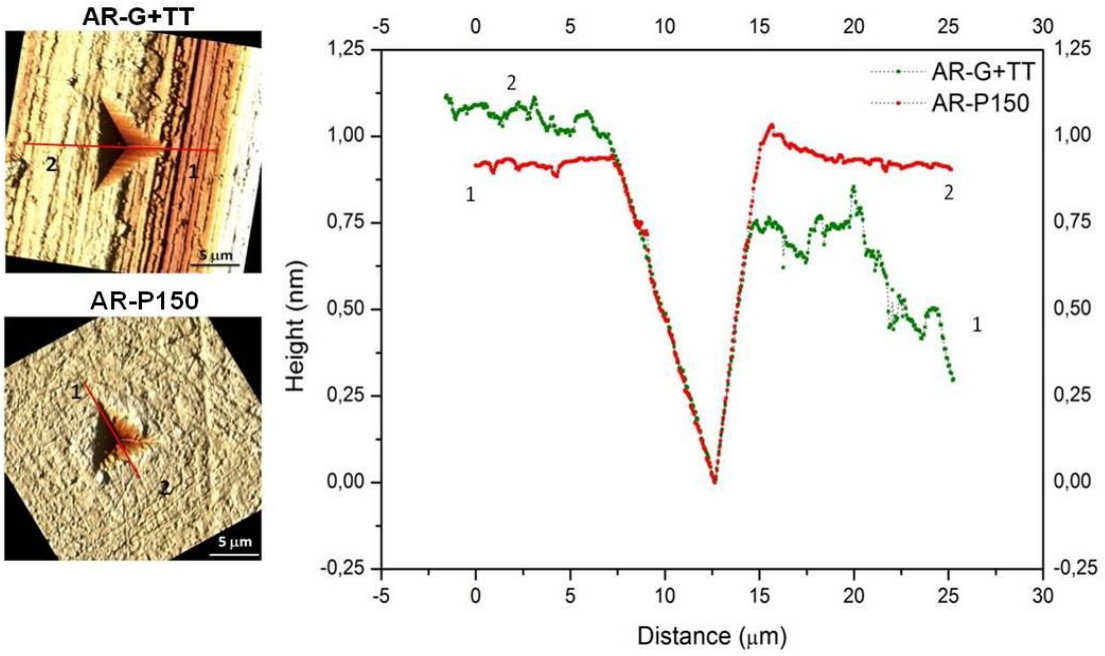


**Figure 4.12**: Cross section profile for the G+TT and $P_{150}$ specimens.

### 4.2.1.3. Nanoscratch

The last experience made in plain view has been nanoscratch testing. It has been done in all the samples in the longitudinal and transversal direction to grinding marks, in order to study if any damage mechanism is activated and at which load is activated.

**Figure 4.13** represents the penetration of the tip as function of the scratched distance in AR-samples. This has been evaluated for all the samples, but there are not all represented given that did not supply additional information. One can observe the difference between the scratch made on the longitudinal and the transversal direction. It may be seen that in all the cases, transversal direction exhibits a deeper penetration. Moreover, it can be seen that for $P_{150}$ and $P_{UPC}$ the response of the material is more homogeneous, whereas G and G+TT the response is very heterogeneous and with a high scatter, especially in the transversal direction. In G+TT, the response changes significantly as a function of the scratch distance, because of roughness of the samples, whereas in $P_{150}$ and $P_{UPC}$ the material is more homogeneous and its roughness is quite flat.

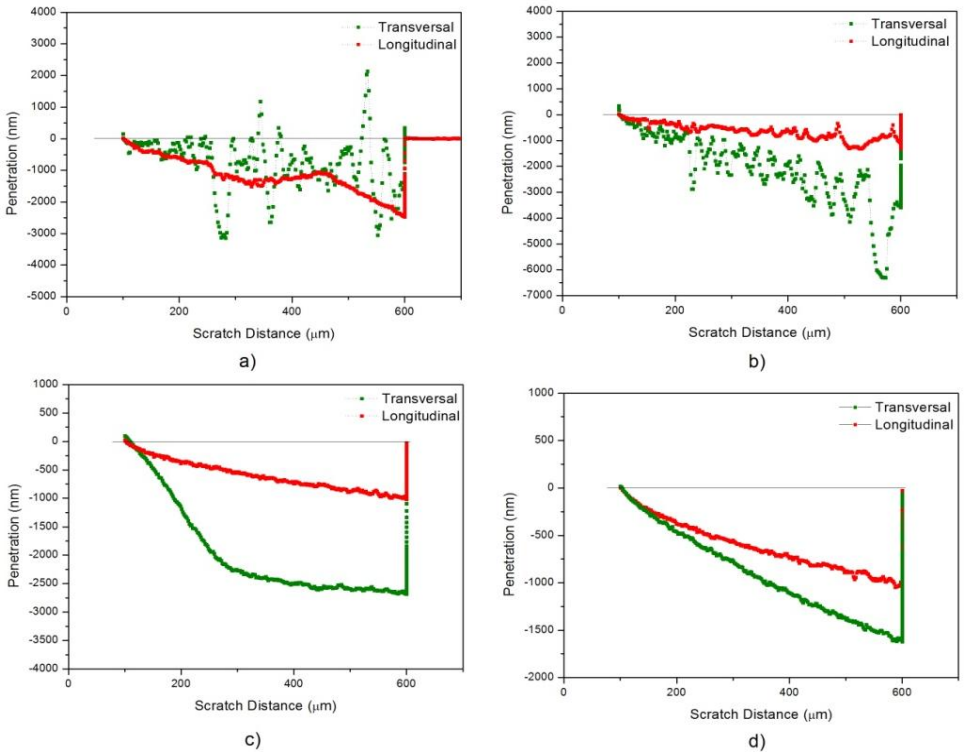


**Figure 4.13**: Results of the nanoscratch test made on AR samples:
(a) G, (b) G+TT, (c) $P_{150}$ and (d) $P_{UPC}$.

**Figure 4.14** shows some of the results of the nanoscratch test done in IE-samples. It may be appreciated that, as occurred in AR, IE-G (**Figure 4.14a**) presents a high scatter due to the roughness and heterogeneous sample, while $P_{UPC}$ (**b**) has a more homogeneous response, similar in both transversal and longitudinal directions, even if on the transversal direction penetration is bigger.

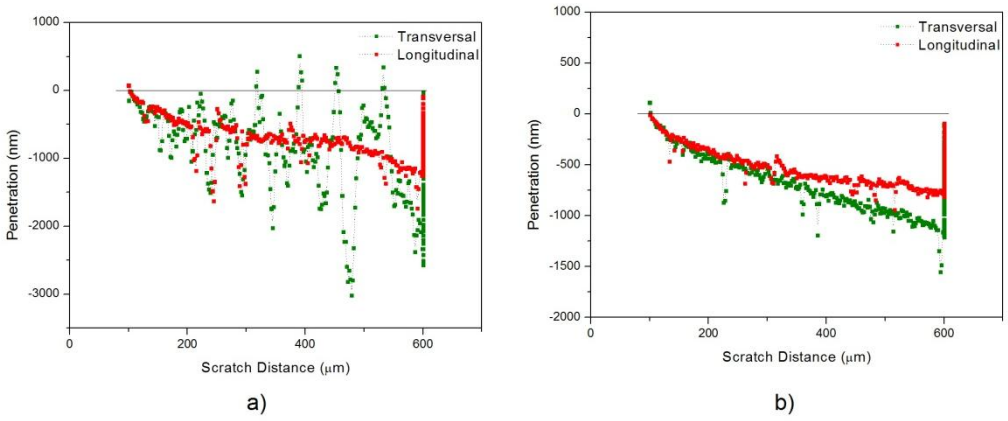


**Figure 4.14:** Results of nanoscratch test made on IE samples:
(a) G and (b) $P_{UPC}$.

Finally, **Figure 4.15** shows some of the results of nanoscratch done on the samples with TiN coating. In this case, both G (**Figure 4.15a**) and PUPC (**b**) present a high scatter given that on the TiN coating there are many artifacts as we commented previously, being the sample more heterogeneous.

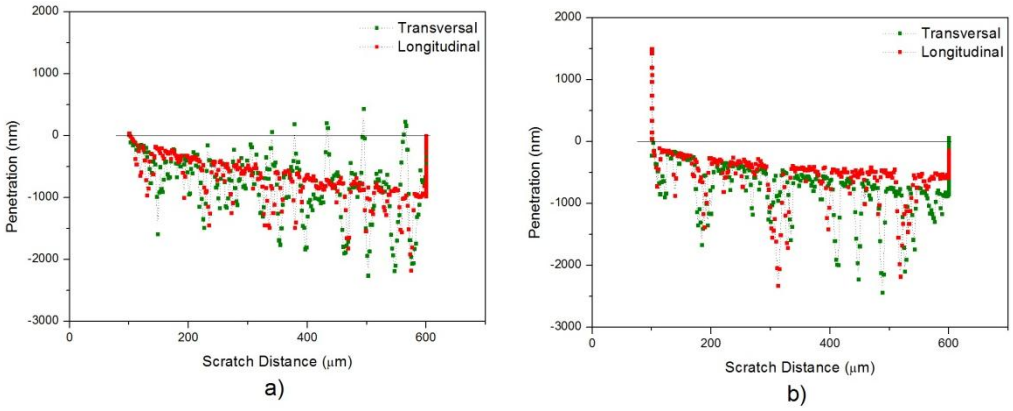


**Figure 4.15:** Results of nanoscratch test made on TiN coating samples:
(a) G and (b) $P_{UPC.}$

All the scratches imprints have been observed with FESEM in order to study if damages mechanisms are (and where) activated during the scratch test and when are activated. **Figure 4.16** shows the scratch track performed on AR-samples on the direction perpendicular to the grinding marks. Differences may be clearly discerned between the samples G and G+TT and the polished samples ($P_{150}$ and $P_{UPC}$). This difference is due to the high roughness of G and G+TT. One can observe some spallation around the nanoscratch track, especially in the samples $P_{150}$ and $P_{UPC}$ (see black arrows). White arrows indicate the sliding direction.

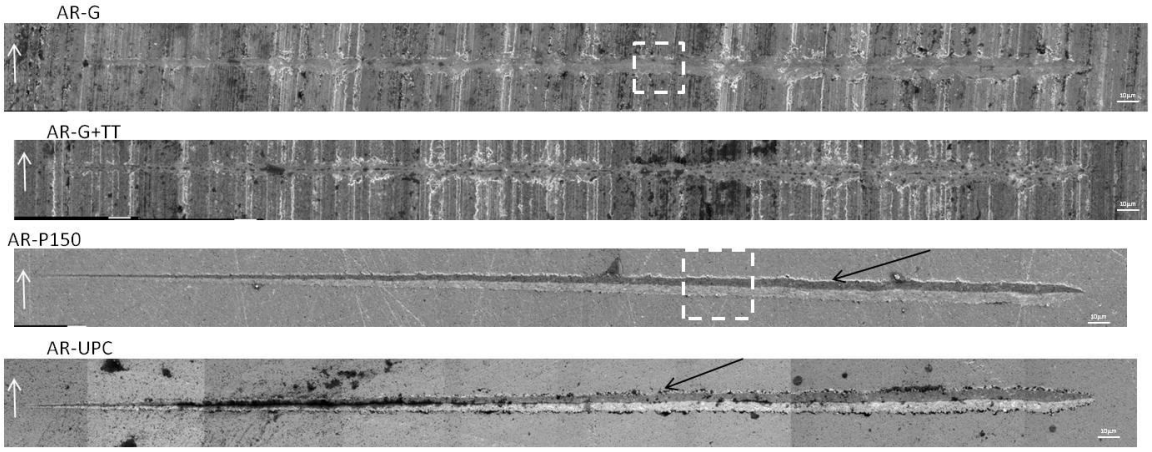


**Figure 4.16:** Scratch test on the direction perpendicular to the grinding marks fon AR-samples. All the samples were observed but not all are shown given that did not provide any additional information.

In **Figure 4.17** is shown a detail of the scratch track for AR-G and AR-$P_{150}$. Microcracks can be observed in the crack track. The presence of two phases and the high heterogeneity of the material complicate the localization of damage mechanisms.

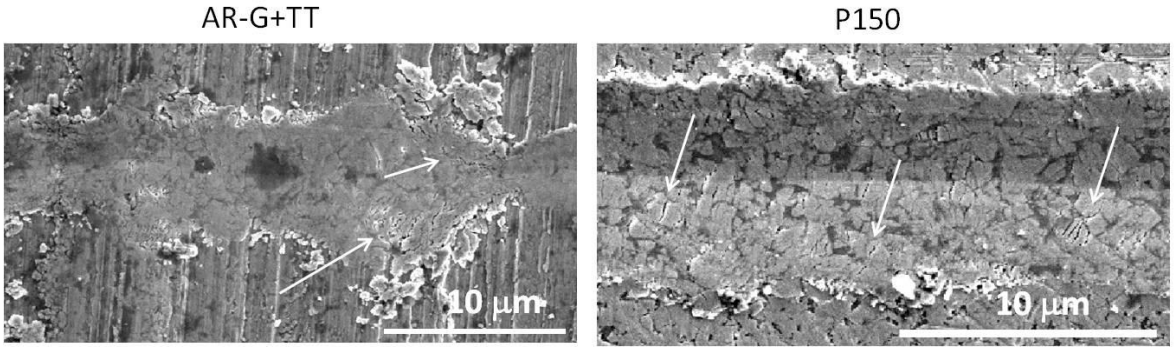


**Figure 4.17:** Detail of the scratch test made in AR-G and AR-$P_{150}$.

**Figure 4.18** shows the scratch track made on the direction of the grinding marks in IE-samples. One can observe that along the nanosracth track it can be appreciated some spallition events (white arrows), being more pronounced for the IE-G and IE-$P_{150}$. This result points out that this phenomenon does not show out for flat or less rough specimens, like IE-$P_{UPC}$.

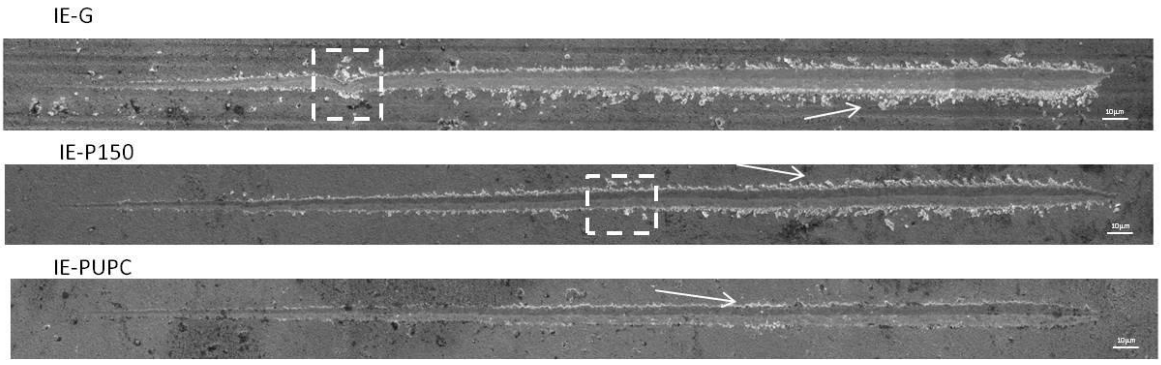


**Figure 4.18**: Scratch track on IE-samples. Scratch made on the direction of the grinding marks. All the samples were observed but not all are shown given that did not provide any additional information

**Figure 4.19** shows a detail of the scratch track. Again, microcracks can be clearly observed on the scratch track.

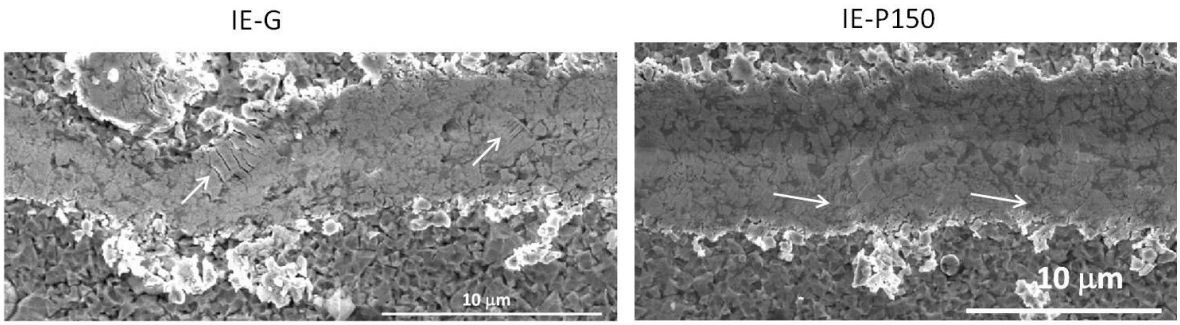


**Figure 4.19:** Detail of the scratch test made on IE-G and IE-P150.

## 4.2.2. Cross-section testing

Experiences made in plain view at micro- and nanometric length scale have proven that roughness plays an important role in assessment of mechanical properties at the surface level. Given that in plain view one obtains an important scatter in results, nanoindentation tests have also been made in cross-section in order to evaluate the different hardness (*H*) and elastic modulus (*E*) trend between the substrate and the coating, aiming to reduce the scatter associated with the superficial roughness. One of the difficulties of this test is the fact that one can only indent once in the coating because it present a thickness of few μm (lower than 5 μm). Moreover, there is some rounding effect in the edge of the samples (at the coating zone) that introduces some scatter in the cross section results.

In **Figure 4.20** it is shown the hardness as a function of the distance (measured since the first nanoindentation). It can be seen that, at first, all the samples have the same *H* (about 25 ± 5 GPa) and same *E* (≈ 500 GPa), what agrees with results presented above (plain view section). At 45 μm it seems that both *H* and *E* increase except $P_{UPC}$ that remains constant given that it has no almost any compression stress or cracks (it is a material without the defects induced by grinding). Near the damaged surface a trend is observed, but the values of *E* are too high for distances over 45 μm, probably because indentation is taking place in the rounding zone, the indenter has slipped or an artifact has been indented (see **Figure 4.23)**.

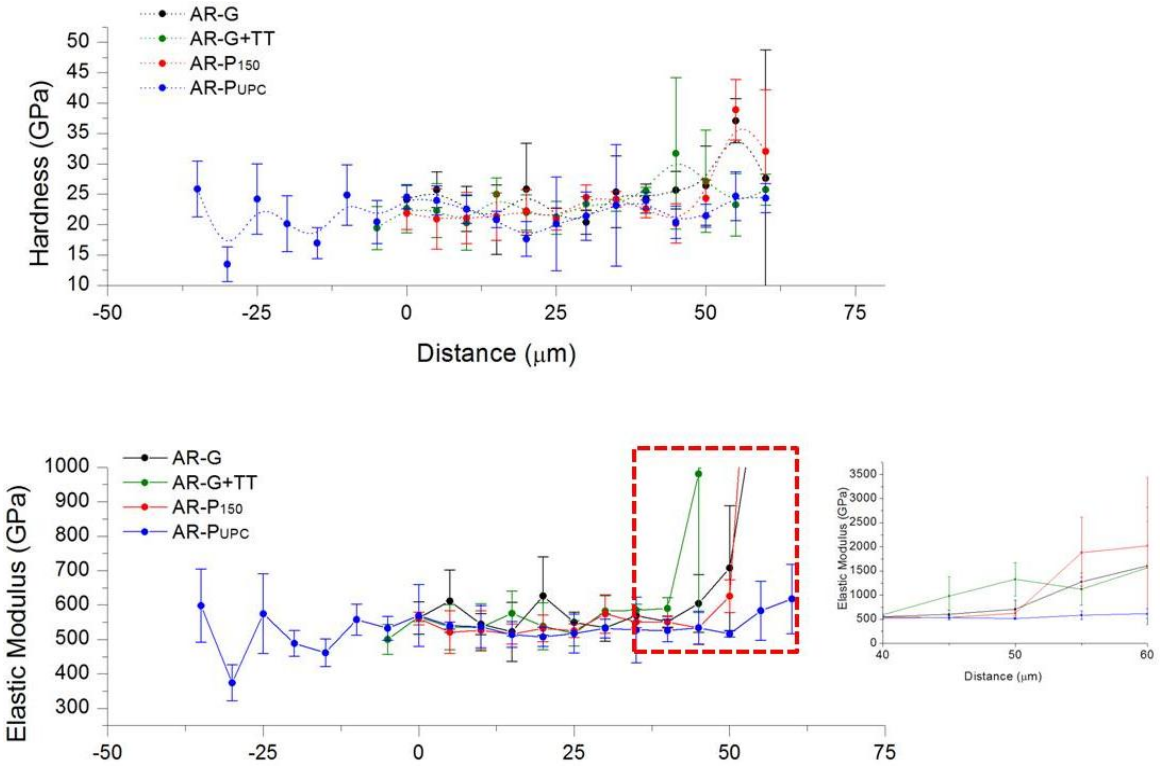


**Image 4.20**: Hardness in function of the distance (measured since the first nanoindentation performed in the region free of defects induced during grounding process).

Nanoindentations have also been done in cross-section for IE-samples and the results are shown in **Figure 4.21**. One can appreciate two different tendencies, one for distances below 112.5 μm and other for distances over 112.5 μm. In the first case can be seen that *H* is almost the same for all the samples (22.5 ± 7 GPa). The same occurs for the elastic modulus (550 ± 100 GPa). For distances over 112.5 μm, there is an important decrease in the values of *H* and *E*, given that the indentation has been made in the Bakelite.

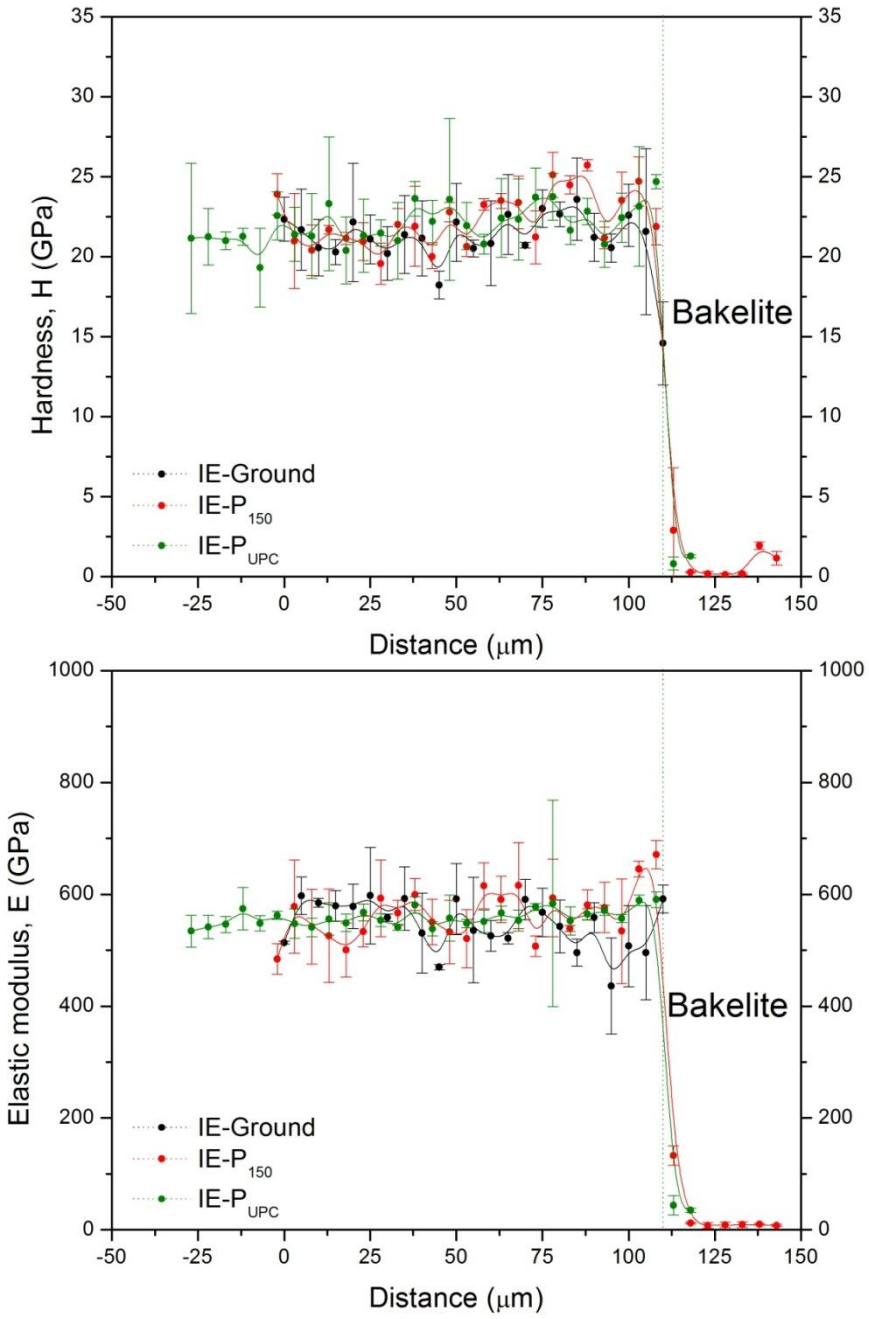


**Image 4.21**: Hardness and elastic modulus as a function of the distance (measured since the first nanoindentation done inside the material free of defect created due to the grounding process).

Finally, **Figure 4.22** shows the results of nanoindentations made in coat-samples. Once more, there are two different tendencies, one for distances below 100 μm and other for distances over 100 μm. In the first case can be seen that the hardness sample is G, then $P_{UPC}$ and lastly $P_{150}$. Moreover, the elastic modulus is almost the same (550 ± 100 GPa).

For distances over 100 μm, there is an important decrease of the mechanical properties due to the imprints where done in the Bakelite.

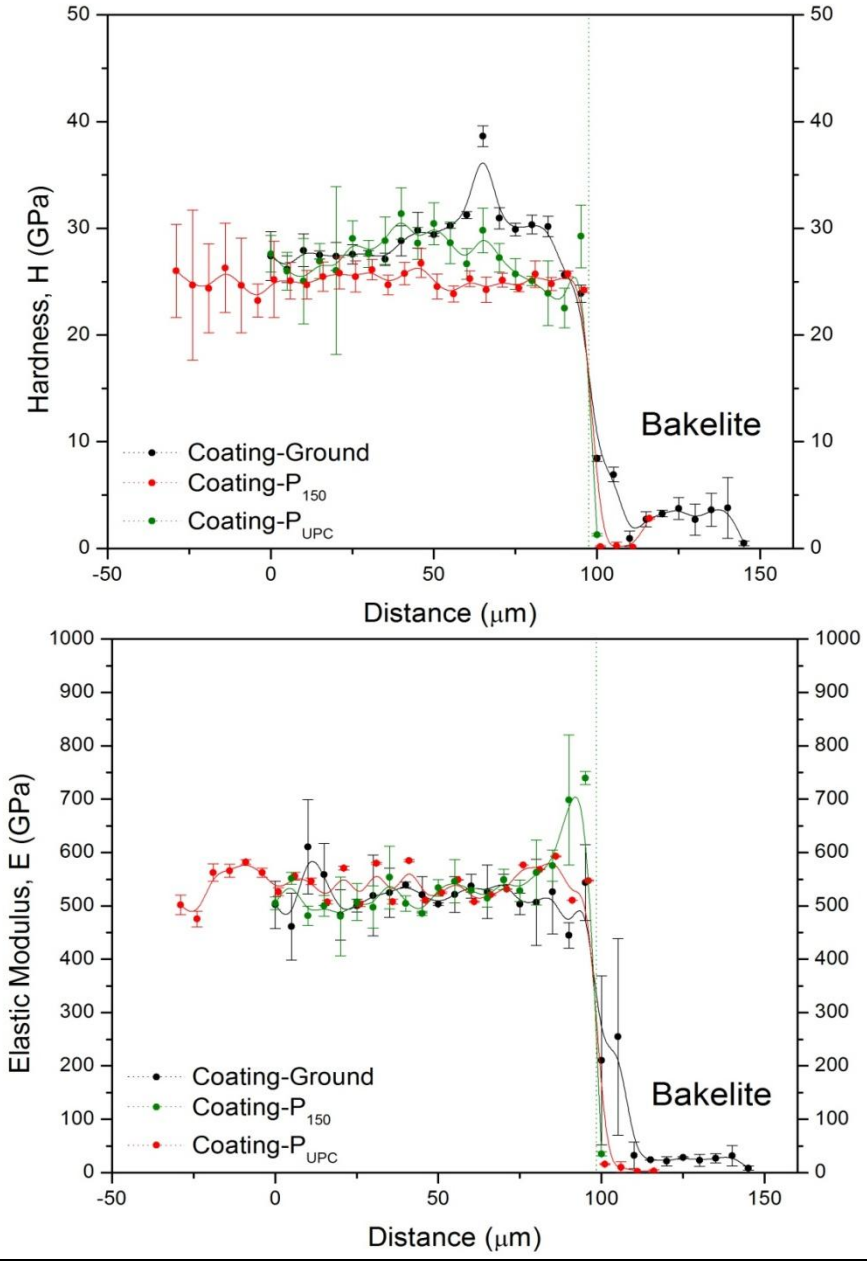


**Image 4.22**: Hardness and elastic modulus as a function of the distance (indentation profile from the material free of induce defects until the bakelite).

Finally, Nanoindentations made on the cross-section have been observed with FESEM in order to ensure that the nanoindentation array has been done properly and that the region with damage has been indented.

In **Figure 4.23** it can be appreciated the pre-existing rounding effect at the edge of the coating thin can introduce an important scatter in the values of H and E. After seeing this effect, all the samples were embedded for obtaining good results.

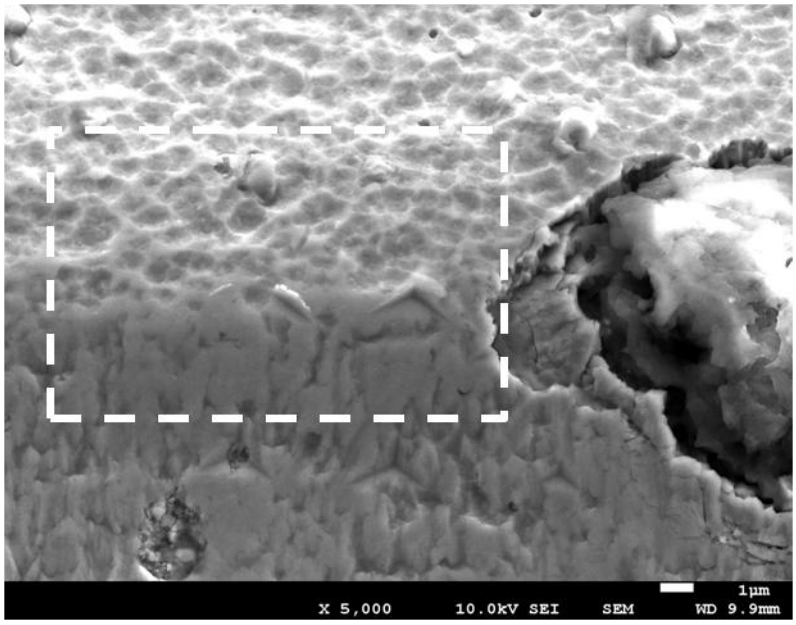


**Figure 4.23:** FESEM image showing the edge side of the specimen.

In **Figure 4.24** one can observe nanoindentations made for the sample AR-G. The reason of the high scatter obtained in **Figure 4.20** at 60 μm may be identified: in the top part of this image one can see that the tip of the nanoindenter slipped (see the white square), causing a sliding of the indenter tip and increasing the scattering associated with this point. This effect can be attributed to a rounding effect of the specimen produced during the sample preparation. Thus, a wrong result for this indentation is obtained. Also, in this image it can be seen the residual imprints done in the region free of defects, some of them marked with a dash white circle.

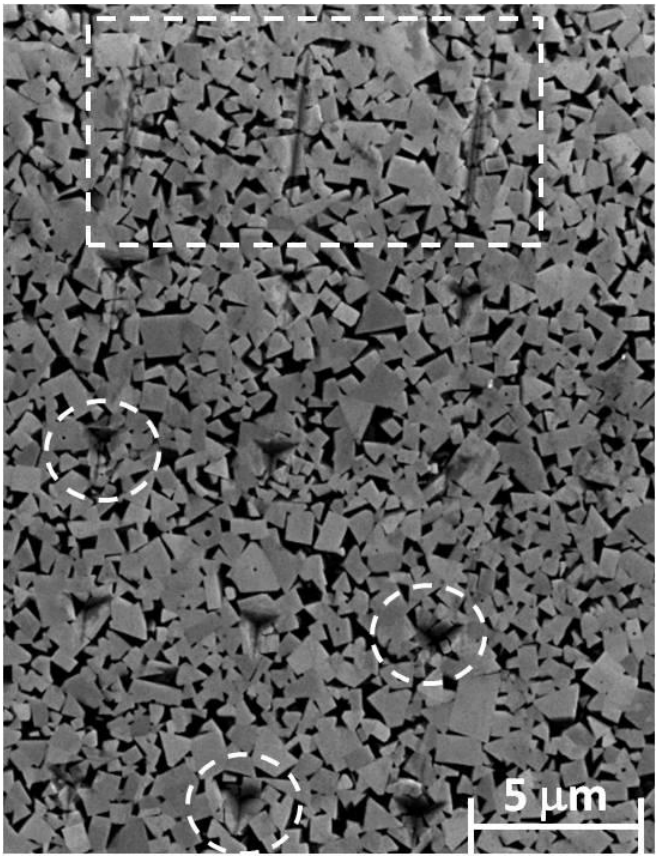


**Figure 4.24** FESEM image of a nanoindentation made on the AR-G sample.

Furthermore, small region of the indentation array done in the coat-$P_{UPC}$ specimen is depicted in **Figure 4.5** As it shows, in that case the flat surface of interest is appropriate for a correct hardness and elastic modulus study. All the samples have been observed but they all are not presented given that these images did not give any additional information.

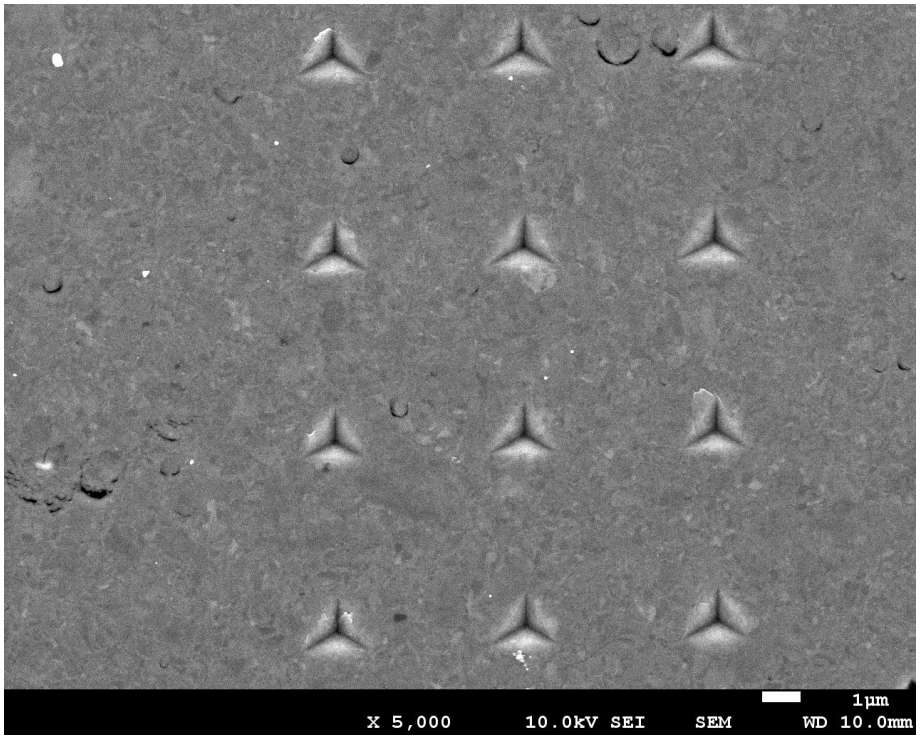


**Figure 4.25**. FESEM image showing part of the indentation array done in cross section for the coat-$P_{UPC}$.

Finally, in order to try to establish a correlation between the mechanical properties and the hardness profile for the AR-G specimen, a sequentially polishing process and nanoindentation tests were done for this specimen for the initial 12 μm.

To study how roughness could influence on mechanical properties, a polishing rate evaluation has been done. In order to estimate the thickness removed during the polishing step, the Vickers imprint prior to polishing (100kgf) have been observed by all along the successive polishing stages. The evolution of the length for the residual indent depth reveals the thickness of the thin layer removed during the polishing. Moreover, the sample has been observed by AFM for different polishing times in order to asses that the superficial roughness started to disappear. As it can be seen in **Figure 4.26,** roughness decreases significantly in just 60 seconds.

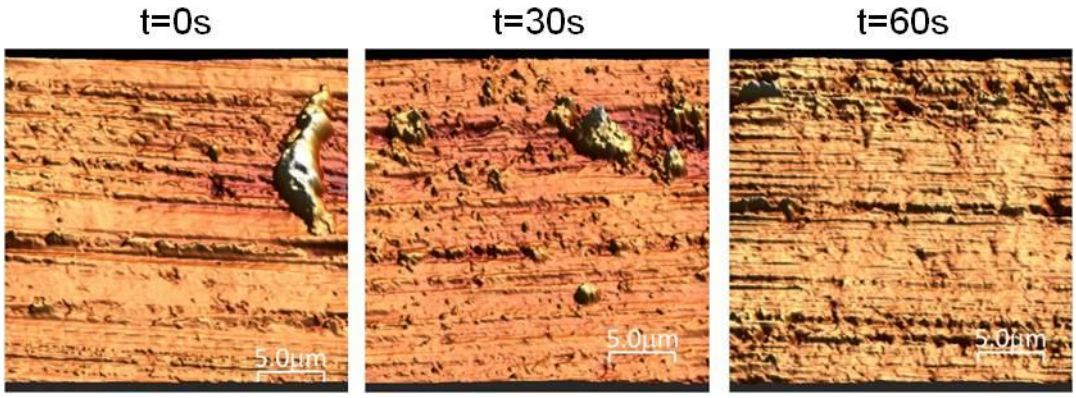


**Figure 4.26:** AFM images (3D view, 25 x 25 $\mu m^2$) of AR-G for different polishing times.

**Figure 4.27** shows the surface profile for AR-G sample at different polishing times. It may be observed that both for *t* = 0s and for *t* = 30s the sample exhibit a relatively high roughness (one cannot see the difference even if one has polished the sample because the sample is highly heterogeneous). However, for *t* = 60s it may be appreciated that the sample has been polished and the profile is flatter.

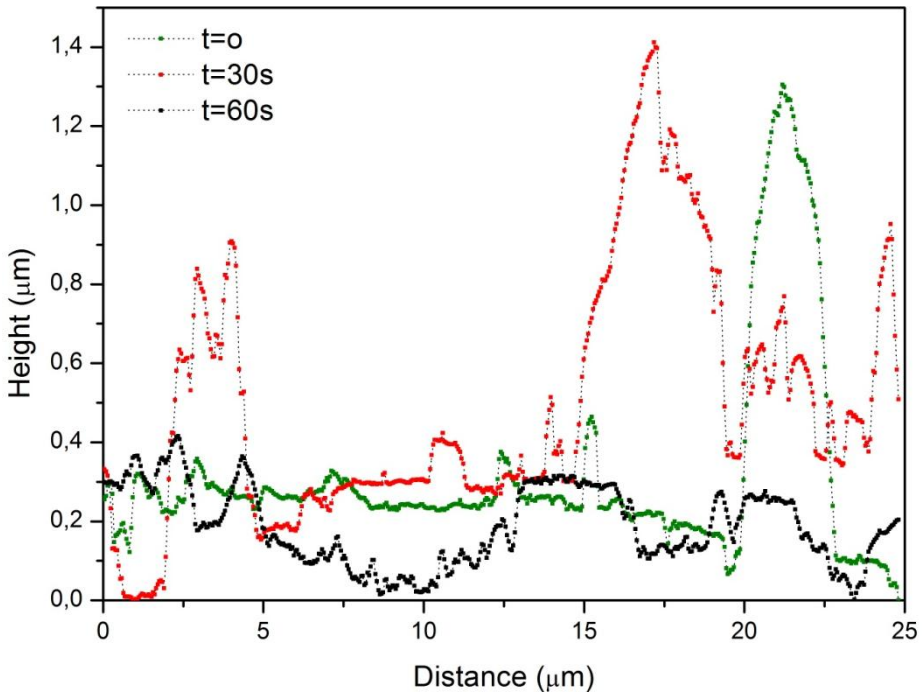


**Figure 4.27:** Surface's profile measured at before starting the polishing rate, after 30s and 60s.

For each polishing step, the micro- and nanomechanical properties have been determined at 2000 and 250 nm of maximum indentation depth, in order to correlate them with the polished length (distance) as depicted in **Figure 4.28**. One can observe that the hardness value in $t$ = 0 s is 18.7, which corresponds to the value of AR-G calculated before and expressed in **Table 4.1**. When 1 μm of material has been removed, $H$ decreases for, after polishing 0.5 μm more, raise again its value. The hardness value remains more or less constant but with a high scattering associated. When one has removed about 5.5 μm, the scattering decreases significantly, given that the roughness has also decreased and the sample is flatter and more homogeneous. This data points out that the scattering associated with hardness values is strongly modified by the superficial roughness.

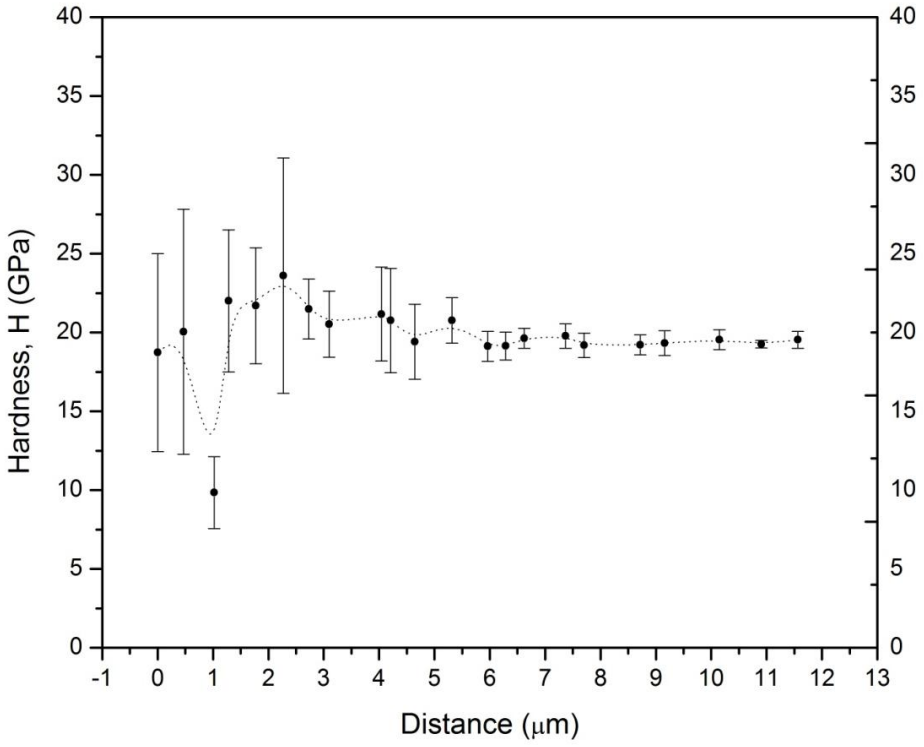


**Figure 4.28:** Hardness and residual stresses as function of the distance or polished length.

The polishing speed has also been calculated and represented as function of the polishing time, see **Figure 4.29**. It can be observed that at the beginning of the polishing rate (little polishing time values) the polishing speed presents high values (130 nm/min). As the sample is polished, the polishing speed decreases. When the sample has been polished during 7500s, the polishing speed increases a little bit and it remains more or less

constant. It is logical to obtain high polishing speeds at the beginning, because there is a lot of roughness and so, one can easily remove material. As the sample is polished it is less roughness and more homogeneous, and so it is harder to remove material of the surface (low values of polishing speed), yielding a polishing speed for a homogeneous WC-Co specimens with 13wt.%Co of around 38 nm per minute.

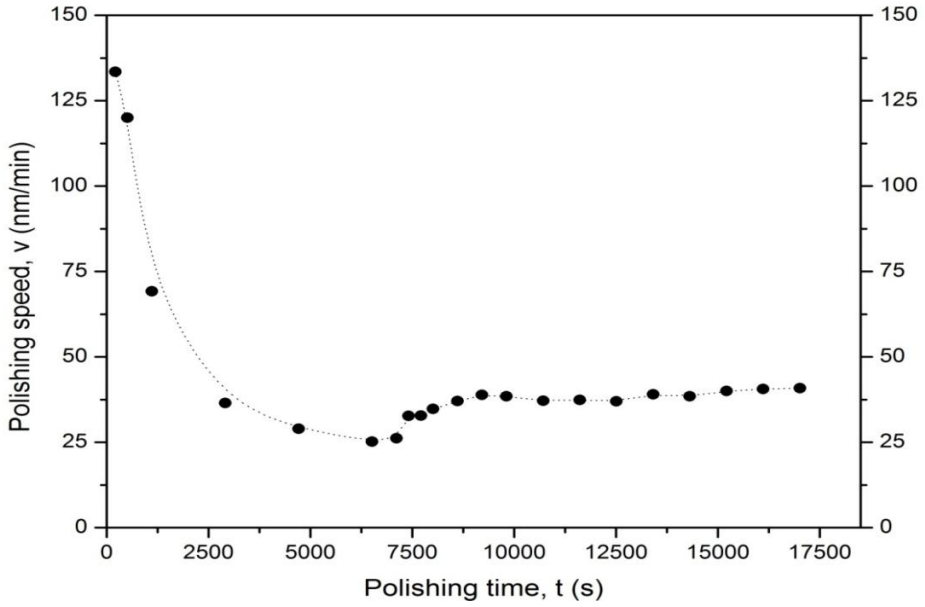


**Figure 4.29**: Polishing speed as function of the polishing time.

After removing the superficial roughness, cracks appeared on the surface around the Vickers' indentation. It can be seen that roughness had masked these cracks, given that for the G sample, any crack was observed as we presented previously **(Figure 4.6)** but, after polishing 8 μm some cracks appeared around the Vickers indentation made as it can be seen in **Figure 4.30** by means of LSCM.

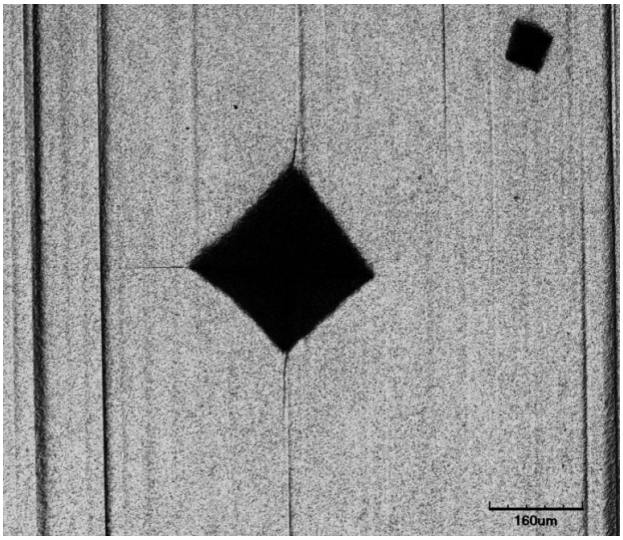


**Figure 4.30:** LSCM showing several radial cracks on the side of the residual Vickers imprint after polishing 8 μm.

# 5. Protocol proposed to mechanical characterization of surface integrity.

After this investigation, the following protocol is proposed to study similar specimens:

1.- Plain view measurements at micrometric length scale. The plastic field is necessary to be confined inside the region where the compressive stresses as well as the damage is confined. It is important to perform the array of indents in the center of the specimen (at least 2 mm from the edges for avoiding the rounding zone).

2.- Observe the residual imprints by any surface analysis technique and FESEM in order to study if any damage mechanism present on the imprint.

3.- Prepare the specimen for cross section measurements:

1- Mount the samples in cross section in bakelite and polish for assuring that the samples are completely flat.
2- Nanoindentation profile from the region free of defects into the damage layer.
3- Observe the nanoindentations by FESEM in order to ensure that imprints have been done correctly and that, at least, one indentation has been made in the surface layer.

4.- If the compressive residual stress has been determine by means of XRD, it is possible to do a successive polishing process determining for each polishing step the nanomechanical response made in plain view. For that reason, it is strickly necessary to determine accurately the polishing speed for each material.

# 6. Conclusions

From this work, the following conclusions can be drawn:

1. It has been found that local mechanical properties at the surface level are highly dependent on the surface roughness.

2. In nanoindentation tests the hardness and elastic modulus is not constant for penetrations depths under 300 nm because the compression stresses as well as the superficial damage are present in the small-scale surface layer.

3. The nanoscratch tests realized on the longitudinal and transversal direction with respect to the grinding marks reflect significant differences: on the transversal direction the penetration of the tip is deeper as well as the scatter on results.

4. Surface damage induced during either grinding or nanoindentation may be masked by the roughness. These cracks can be observed after removing the initial 5 μm, where the maximum residual stresses are concentrated.

5. Cross-section results were not effective for providing any additional information, although the scatter clearly decreases.

6. A protocol to characterize surface damage (see section 5) has been proposed.

# 7. Proposals for futures studies

- In order to decrease the scatter obtained in the nanoindentations realized, tests could be done with a DCM tip, whose tip's radius is 10 nm (the tip used on the nanoindentations realized for this project had a radius of 250 nm). If the radius decreases, the indentations can be done at 300 nm of distance, which represents one fifth of the current distance. However, problems related with the scale effect may appear using a DCM tip.

- Study the cohesion of the TiN coating in cross section. For this study, Coat-samples should be polished and a nanoscratch test should be done on the edge of the samples, where there would be a TiN layer.

- Finally, in order to clearly extract the mechanical properties (hardness and elastic modulus) for the superficial region where residual stresses and microcracks are located, it will be possible to observe this region by nanovision before performing the indentation process.

# 8. Environmental impact

During this study, sample preparation activities have involved the use of considerably quantity of distilled water, polishing lubricant and solvent. However, laboratory supplies consumption together with energy consumption does not imply an environmental risk and/or deep impact in environmental areas. Indeed, all research activities has been conducted by proper management of solid and liquid waste which have been framed within institutional and EU environmental policies.

In general terms, this project has a positive indirect environmental impact over natural resources; in this case tungsten and cobalt which are used to produce hardmetals. The results obtained through this research will permit to understand how does surface compressive stresses and microcracks on the surface influence on cemented carbide mechanical properties, and so one will be able to improve tools designs and optimize natural resources required in its production.

# 9. Economical cost

| Item | Unit cost | Quantity | Subtotal (€) |
|---|---|---|---|
| **Cost of the machines** | | | |
| Polishing Machine | 15 €/h | 25 | 375 |
| Vickers test | 25 €/h | 4 | 100 |
| Nano-indentation machine | 40 €/h | 15 | 600 |
| AFM | 50 €/h | 20 | 1000 |
| AFM tips | 18 €/unit | 2 | 36 |
| Confocal microscope | 30 €/h | 8h | 240 |
| FESEM | 120 €/h | 80h | 9600 |
| **Subtotal** | | | **11951** |
| **Laboratory material** | | | |
| Polishing cloths | 100 €/unit | 3 | 300 |
| Diamond past | 300 €/unit | 0.5 | 150 |
| Lubricant | 50 €/l | 0.5 l | 25 |
| Polifast resin | 50€/u | 1 | 50 |
| Acetone | 2 €/l | 4 l | 8 € |
| **Subtotal** | | | **533** |
| **Timetable of the specialised personnel (5months)** | | | |
| Junior Engineer | 20 €/h | 800 | 16000 |
| Chief project | 60 €/h | 40 | 2400 |
| Laboratory technician | 40 €/h | 40 | 1600 |
| **Subtotal** | | | **20000** |
| **TOTAL COST OF THE PROJECT** | | | **32484** |

# 10. Acknowledgements

This research was partly a collaborative Industry-University program between Seco Tools and Universitat Politècnica de Catalunya, through the Centre d'Integritat Estructural i Fiabilitat dels Materials (UPC-CIEFMA). In particular, Seco Tools kindly supplied the experimental hardmetals grades studied in this investigation.

I would like to extent my gratitude to Luis Llanes for his effective guidance and support. I am also sincerely thankful for the kind assistance provided by Joan Josep Roa, indeed, the most important support that I have encountered during my project.

Last but not least, the technical assistance of Isaac López and Francesc Heredero is highly appreciated.

# 11. References

[1] www.sandvik.com, visited 19/04/14.

[2] V. V. Álvarez (**2012**), "Fatigue behavior and associated binder deformation mechanisms in WC-Co cemented carbides", Master thesis, UPC.

[3] T. A. Rodil (**2006**), "Edge effect on abrasive wear mechanisms and wear resistance in WC-6 wt.%Co hardmetals", PhD Thesis, Karstad University.

[4] http://www.e6.com, visited 22/04/14.

[5] H. Kolaska (**1992**), "Pulvermetallurgie der hartmetalle", Fachverband für Pulvermetallurgie, Hagen (Germany).

[6] http://nanopartikel.info/en/nanoinfo/materials/tungsten-carbide-cobalt, visited 02/05/14.

[7] H. O. Pierson (**1992**), "Handbook of Chemical Vapor Deposition (CVD): Principles, Technology, and Applications". William Andrew Inc; pp. 147-177. ISBN 0-8155-1300-3.

[8] J. Nerz *et al.* (**1992**), "Microstructural evaluation of tungsten carbide-cobalt coatings". *Journal of Thermal Spray Technology* 1:147–152.

[9] G.S.Upadhyaya (**1998**), "Cemented Tungsten Carbides: Production, Properties and Testing", Noyes Publications, pp. 227-253. ISBN: 0815514174.

[10] C.M. Fernandes *et al.* (**2011**), Cemented carbide phase diagrams: A review. *International Journal of Refractory Metals and Hard Materials,* 29:405.

[11] Z. Yao *et al.* (**1995**), **"**Nano-grained Tungsten Carbide-Cobalt (WC/Co)", *Materials Modification Inc.*

[12] U. Schleinkofer *et al*. (**1996**), "Fatigue of hard metals and cermets," *Materials Science and Engineering*: A, 209:313-317.

[13] http://www.scsaws.co.uk, visited 28/06/2014.

[14] E. Altuncu *et al.* (**2013**), "Cutting-tool recycling process with the zinc-melt method for obtaining thermal-spray feedstock powder (WC-Co)". *Materials and technology,* 47:115–118.

[15] http://www.allaboutcementedcarbide.com/01_03.html, visited 15/05/2014.

[16] A. C. Fischer-Cripps (**2004**), "Nanoindentation". Springer 2nd ed. pp. 21-37; ISBN: 0-387-22045-3.

[17] M.F. Doerner *et al.* (**1980**), "A method for interpreting the data from depth-sensing indentation instruments". *Journal of Materials Research*, 1:601-609.

[18] www.agilent.com, visited 17/07/2014.

[19] http://cp.literature.agilent.com/litweb/pdf/5990-4907EN.pdf, visited 10/06/2014.

[20] E.G. Herbert *et al*. (**2001**), "On the measurement of stress–strain curves by spherical indentation". *Thin Solid Films* 331:398-399 .

[21] J.J. Roa (**2010**), "Mechanical properties of HTSC at micro/nanometric scale", PhD Thesis, UB.

[22] I. C Albayrak et al (**2010**), "Elastic and mechanical properties of polycrystalline transparent yttria as determined by indentation techniques*"*. *Journal of the American Ceramic Society*, 93:2028-2034.

[23] W.C. Oliver *et al.* (**1992**), "An improved technique for determining hardness and elastic modulus using load and displacement sensing indentation experiments". *Journal of Materials Research,* 7:1564-1583.

[24] L. Han *et al*. (**2009**), "Determining the elastic modulus and hardness of an ultrathin film on a substrate using nanoindentation". *Journal of Materials Research,* 24:1114-1126.

[25] W.C. Oliver *et al.* (**2004**), "Measurement of hardness and elastic modulus by instrumented indentation: advances in understanding and refinements to methodology". *Journal of Materials Research,* 19**:**3-20.

[26] http://www.csm-instruments.com, visited 22/04/14.

[27] http:// www.coatingspromag.com, visited 30/06/2014.

[28] S. W. Youn *et al.* (**2006**), "Effect of nanoscratch conditions on both deformation behavior and wet-etching characteristics of silicon (100) surface", *Wear,* 261:328-337.

[29] Standard Test Method for Adhesion Strength and Mechanical Failure Modes of Ceramic Coatings by Quantitative Single Point ScratchTesting. ASTM C16-26-05 (**2010**).

[30] E. Rayón et al (**2011**), "Hardness and Youngs modulus distributions in atmosperic plasma sprayed WC-Co" *Surface & Coatings Technology,* 205:4192-4197.

[31] B. Roebuck *et al.* (**2009**), "A national measurement good practice guide-Mechanical Tests for Hardmetals", Teddington, Middlesex.

[32] J.J. Roa *et al.* (**2014**), "Contact damage and fracture micromechanisms of multilayered TiN/CrN coatings at micro- and nano-length scale", *Thin Solid Films,* DOI.

[33] http://www.secotools.com, visited 26/06/2014.

[34] C.A Botero *et al*. (**2014**), "Nanoindentation and nanoscratch properties of mullite-based environmental barrier coatings: Influence of chemical composition – Al/Si ratio". *Elsevier, Surface & Coatings Technology,* 239:49-57.

[35] N. S. Claxton *et al.* (**2005**), "Laser Scanning Confocal Microscopy"; Department of Optical Microscopy and Digital Imaging, National High Magnetic Field Laboratory, Florida State University.

[36] http://http://bahadorimehr.blogspot.com.es/2010/07/sem-fesem.html, visited 23/04/14.

[37] M. Wink (**2011**), "An Introduction to Molecular Biotechnology: Fundamentals, Methods and Applications". Wiley-Blackwell 2nd ed. pp.197-210. ISBN: 978-3527326372.

[38] I. Horcas et al **(2007)**, "WSXM: A software for scanning probe microscopy and a tool for nanotechnology". *Review of Scientific Instruments* 78:013705/8.

[39] J. Yang (**2014**), PhD thesis. Research in progress.